Radiative forcing of anthropogenic aerosols on cirrus clouds using a hybrid ice nucleation scheme

Jialei Zhu[1,2] and Joyce E. Penner[2]

1 Institute of Surface-Earth System Science, School of Earth System Science, Tianjin University, Tianjin 300072, China

2 Department of Climate and Space Sciences and Engineering, University of Michigan, Ann Arbor, Michigan 48109, USA

Corresponding Author: Jialei Zhu (Email: zhujialei@tju.edu.cn)

Abstract

Anthropogenic aerosols impact cirrus clouds through ice nucleation, thereby changing the Earth's radiation budget. However, the magnitude and sign of anthropogenic forcing in cirrus clouds is still very uncertain depending on the treatments for ice nucleating particles (INPs), for haze particle freezing, and the ice nucleation scheme. In this study, a new ice nucleation scheme (hereafter the HYBRID scheme) is developed to combine the best features of two previous ice nucleation schemes, so that global models are able to calculate the ice number concentration in both updrafts and downdrafts associated with gravity waves and has a robust sensitivity to the change of aerosol number. The scheme is applied in a box model, and the ice number concentrations (9.52 ± 2.08 L^{-1}) are somewhat overestimated but are in reasonable agreement with those from an adiabatic parcel model (9.40 ± 2.31 L^{-1}). Then, the forcing and cloud changes associated with changes in aircraft soot, sulfur emission and all anthropogenic emissions between the preindustrial (PI) period and the present day (PD) are examined using the

CESM/IMPACT global model with the HYBRID scheme. Aircraft soot emissions decrease the global average ice number concentration (Ni) by $-1.0\pm2.4\times10^7$ m^{-2} (-1%) (over the entire column) due to the inhibition of homogeneous nucleation and lead to a radiative forcing of -0.14 ± 0.07 W m^{-2}, while the increase in sulfur emissions increases the global average Ni by $7.3\pm2.9\times10^7$ m^{-2} (5%) due to the increase in homogeneous nucleation and leads to a radiative forcing of -0.02 ± 0.06 W m^{-2}. The possible effects of aerosol and cloud feedbacks to the meteorological state in remote regions partly contribute to reduce the forcing and the change in Ni due to anthropogenic emissions. The radiative forcing due to all increased anthropogenic emissions from PI to PD is estimated to be -0.20 ± 0.05 W m^{-2}. If newly formed secondary organic aerosols (SOA) act an INPs and inhibit homogeneous nucleation, the Ni formed from heterogeneous nucleation is increased. As a result, the inclusion of INPs from SOA increases the change in Ni to $12.0\pm2.3\times10^7$ m^{-2} (9%) and increases (makes less negative) the anthropogenic forcing on cirrus clouds to -0.04 ± 0.08 W m^{-2} from PI to PD.

1. Introduction

Atmospheric aerosol loading has increased significantly since the PI period, mainly due to anthropogenic emissions associated with the burning of fossil fuels and biomass. Most studies to date have focused on how the increase in anthropogenic aerosols impacts climate via warm clouds thereby exerting a net cooling effect (Wang and Penner, 2009; Zhu et al., 2019; Gordon et al., 2016; IPCC, 2013). Compared to warm clouds, there has been much less attention paid to anthropogenic forcing as a result of changes to cirrus clouds, which is one of the least understood processes in the climate system (Fan et al., 2016). Cirrus clouds cover about 30% of the Earth's area (Wang et al., 1996) and play an important role in the Earth's

radiation budget and also influence global precipitation and the hydrologic cycle (Waliser et al., 2009; Hong et al., 2016; Matus, A. V. and L'Ecuyer 2017). Ice particles in cirrus clouds are nucleated on aerosol particles, so that changes to the aerosol composition and loading may alter cirrus clouds by altering cloud microphysics, resulting in a cirrus cloud radiative forcing.

There are major uncertainties in calculating the radiative forcing of cirrus clouds using global climate models, both in terms of its magnitude (since PI) and its sign (Storelvmo, 2017). The ice particles in the cirrus clouds can form either by homogeneous freezing of solution droplets (or haze particles) (Koop et al., 2000) or by heterogeneous nucleation of INPs (Cantrell and Heymsfield, 2005). Supercooled aqueous solutions such as sulfate haze particles can form ice through homogeneous nucleation when the relative humidity with respect to ice (RHi) is high (of order 150%), which may be the dominant mechanism for the ice formation in cirrus clouds (Hendricks et al., 2011; Kuebbeler et al., 2014; Penner et al., 2018). However, heterogeneous ice nucleation of INPs formed from dust, soot and other insoluble aerosols requires much lower RHi, so that heterogeneous nucleation is able to occur in advance of homogeneous nucleation in a rising air parcel (Hoose and Möhler, 2012). As a result, heterogeneous and homogeneous ice formation compete for the available water vapor. Heterogeneous nucleation can lead to a significant reduction of the number of ice particles that form compared to homogeneous freezing because the number of INPs is much smaller than the number of haze particles. However, if additional INPs are added to a region where heterogeneous nucleation already dominates, an increase in ice crystal number is expected. Therefore, the radiative effect of aerosols on cirrus clouds could differ in both magnitude and sign depending on the competition between these two ice nucleation processes. Ice nucleation by

INPs vs haze freezing is determined by both the number of homogeneous and heterogeneous ice nucleating particles as well as the updraft velocity or cooling rate.

Despite the relatively low level of understanding of ice nucleation, a few physically based parameterizations that treat the competition between homogeneous and heterogeneous nucleation have been developed in order to study the effect of ice nucleation in global climate models (Liu and Penner, 2005; Kärcher et al., 2006; Barahona and Nenes, 2008). The Liu and Penner (2005) parameterization (hereafter LP) is derived from fitting the simulation results of an adiabatically rising cloud parcel (Liu and Penner, 2005). The LP parameterization is only able to treat cases for which the updraft velocity is positive, so the evaporation of drops during downdrafts is neglected. The parameterization developed by Barahona and Nenes (2008) (hereafter BN) is derived from an analytical solution of the cloud parcel equations (Barahona and Nenes, 2008). The LP and BN parameterizations always show a similar trend when there is an increase in either the haze aerosol number concentrations or INPs, (Shi and Liu, 2018) and they result in very similar ice number concentrations when the water vapor accommodation coefficient is set to 0.1 (Zhou et al., 2016). The Kärcher et al. (2006) parameterization (hereafter KL) explicitly calculates the evolution of ice supersaturation in a rising cloud parcel when different aerosol types freeze (Kärcher et al., 2006). The KL parameterization was used in previous studies of the effect of aerosol particles on cirrus clouds because it includes an explicit representation of the relevant physics (Penner et al., 2009; Penner et al., 2018) and Penner et al. (2018) added the capability to represent evaporation of water in downdrafts. However, in the KL parameterization, aerosol particles in different size bins will freeze chronologically from the largest size bin until the rate at which RHi decreases by water vapor deposition equals the rate at which RHi increases as a result of temperature decreases. Under this assumption,

competition among different aerosol size bins for water deposition is not allowed. As a result, the homogeneous freezing of some particles in small size bins is underestimated in KL parametrization (Liu and Shi, 2018). The KL parametrization results in a smaller sensitivity to increases in sulfate aerosol number than the LP and BN parametrizations except at very low sulfate number concentrations, while the three parameterizations have similar sensitivity to the number concentration of INPs (Shi and Liu, 2018).

Global numerical simulation experiments of aerosol effects on cirrus cloud formation have been carried out in a limited number of studies with different ice nucleation parameterizations and updraft treatments. Penner et al. (2009) used the KL and LP parameterizations to estimate the radiative forcing of aerosols on cirrus clouds using an off-line ice nucleation and radiative transfer model. They found a negligible forcing from sulfate but a significant cooling (ranging from -0.38 to -0.56 W m^{-2}) from surface-based and aircraft emissions of soot with the assumption that 100% of soot particles are efficient INPs (Penner et al., 2009). As a result, the radiative forcing of all anthropogenic aerosols was estimated to be -0.53 to -0.67 W m^{-2} using the LP and KL parameterizations. However, observations later indicated that only 0.01 to 0.1% of the less-hygroscopic soot from fossil fuels and biomass fires act as good INPs at supersaturations near 140% RHi and low temperatures (Koehler et al., 2009; Pratt et al., 2011; Prenni et al., 2012). Gettelman et al. (2012) used the LP and BN parameterizations and calculated that the radiative forcing associated with aerosol effects on cirrus clouds is 0.27±0.10 W m^{-2} (the uncertainty is the standard deviation of the interannual variations hereafter) as a consequence of increasing anthropogenic sulfur emissions (with no effect from soot) (Gettelman et al., 2012).

In addition to assumptions of the extent to which soot might act as an INP, a second source of uncertainty in the calculation of aerosol forcing in cirrus clouds is the treatment of the sub-grid scale updraft velocity used in the nucleation scheme (Zhou et al., 2016). Penner et al. (2009) used a normal probability distribution with a standard deviation of 0.33 m s^{-1} (Penner et al., 2009) while Wang and Penner (2010) used a single updraft velocity based on the standard deviation of mesoscale temperature fluctuations associated with gravity waves (Wang and Penner, 2010). Other models chose a sub-grid scale updraft velocity associated with the predicted turbulent kinetic energy (Liu et al., 2012; Kärcher and Lohmann, 2002; Lohmann, 2002; Lohmann et al., 1999). Joos et al. (2008) added the effect of the contribution of orographic waves to the vertical velocity. Penner et al. (2018) first used a wave spectrum (instead of a constant updraft velocity) together with the KL parameterization to treat the formation of ice crystals. They used the equatorial spectrum of observed gravity waves presented by Podglajen et al. (2016) together with the seasonal and latitudinal variations determined by Gary (2006) and Gary (2008). They also varied the standard deviation from Podglajen et al. (2016) based on the vertical stratification of atmospheric stability, the atmospheric density and topography. However, the radiative forcing of sulfate as well as all anthropogenic aerosols were not explored due to the deficiencies in the KL parameterization (Liu and Shi, 2018).

Secondary organic aerosols (SOA) have been shown to have a highly viscous semisolid or even glassy state at low temperatures and low RHi in many experiments (Koop et al., 2011; Pajunoja et al., 2014; Renbaum-Wolff et al., 2013; Saukko et al., 2012). Observations also found SOA acting as IN and in the ice crystal residues of cirrus clouds (Ignatius et al., 2016; Wagner et al., 2017; DeMott et al., 2003; Cziczo et al., 2013; Wilson et al., 2012). A peak in the number concentration of ultrafine

153   particles were observed near 12km in the Amazon and identified as primarily organic.

154   Furthermore, a marker molecule indicated that a substantial fraction of the organics

155   in aerosol-rich layers in the upper troposphere were associated with the oxidation of

156   isoprene (Andreae et al., 2018). A modelling study that included the nucleation of

157   new particles through organic nucleation predicted that there are a large number of

158   accumulation mode SOA particles existing in the upper tropical troposphere which

159   may be important for the ice nucleation (Zhu and Penner, 2019). SOA particles have

160   a strong potential to act as INPs to form ice particles via heterogeneous freezing

161   under the conditions conducive to ice formation in the upper troposphere (Knopf et

162   al., 2018). However, the influence of SOA on cirrus clouds is not yet fully studied

163   (but see Penner et al., 2018).

164   In this study, we combined the best features of the LP and KL parameterizations

165   to develop a hybrid ice nucleation scheme that accounts for the changes in ice

166   number concentrations in both the updrafts and downdrafts associated with a

167   spectrum of gravity waves. Using a global climate model coupled with the new ice

168   nucleation scheme, the radiative forcing of aircraft soot and sulfate were examined.

169   Furthermore, the radiative forcing of anthropogenic aerosols on cirrus clouds since

170   the PI time period was estimated both including and excluding the effect of changes

171   in SOA. A global average negative anthropogenic forcing of -0.20±0.05 W m^{-2}

172   without SOA as a result of aerosol effects in cirrus clouds is suggested. The forcing

173   is reduced to -0.04±0.08 W m^{-2} when SOA is included.

174

2. Methodology

2.1 Model

We used the Community Earth System model (CESM) version 1.2.2 (refer to http://www.cesm.ucar.edu/models/cesm1.2/ for details) coupled to the University of Michigan IMPACT aerosol model (Liu et al., 2005 with updates as described herein) with a resolution of 1.9° (longitude)×2.5° (latitude) and 30 vertical layers to simulate aerosols and their effects on cirrus clouds. This version of the IMPACT model simulates the number and mass of pure sulfate in three modes (i.e. nucleation (<5 nm), Aitken (5-50 nm) and accumulation (>50 nm)) and their interaction with the following fourteen other aerosol species/types. Sulfate is the only aerosol participating in homogeneous ice nucleation in the model. Soot from fossil fuel and biofuel burning (fSoot) is simulated in three modes with different hygroscopicity according to the number of monolayers sulfate on its surface (Yun et al., 2013) while soot from biomass burning (bSoot) is simulated in one mode. 0.05% of fSoot with <1 monolayers of sulfate and 0.1% of fSoot coated with 1-3 monolayers of sulfate as well as 0.1% of bSoot are assumed to be effective INPs. The hygroscopicity of fSoot and bSoot is determined by volume averaging the hygroscopicity of the underlying particles and the number of sulfate monolayers on the particles. Aircraft soot is simulated in two modes. The first mode has acted as an ice nuclei within contrails that subsequently evaporated (cSoot). The 2nd mode which has not been an ice nuclei within contrails is not considered to act as an INP in the model. The soot that has already been included in contrail ice is pre-activated. We assume the pre-activated aircraft soot coated with less than 3 monolayers of sulfate to be an INP similar to the treatment in Zhou and Penner (2014) (see also Mahrt et al., 2019). Dust and sea salt are each carried in four separate bins with varying radii. Dust with fewer than 3 monolayers of sulfate coating is used to form heterogeneous INP in the model.

This treatment is consistent with the results of field studies by DeMott et al. (2003), Cziczo et al. (2004) and Richardson et al. (2007). The assumptions for aerosols to be effective INPs in the model are summarized in Table 1. The aerosols simulated by the IMPACT model are only able to nucleate the initial ice crystal number concentration in cirrus clouds in the CESM model. Thereafter, the growth and sedimentation as well as evaporation of ice crystals follow the treatment in the CESM. In addition, the changes to cirrus clouds have feedbacks as a result of changes to the radiation budget, temperature, and the formation of warm clouds, as simulated in the CESM model.

2.2 Ice nucleation parameterization

The LP parameterization is only able to calculate the ice nucleation in a rising parcel, but is not able to predict the changes in the supersaturation or simulate the evaporation of ice in downdrafts. As a result, the scheme used by Penner et al. (2018) to treat gravity waves cannot be used with the LP parameterization as it was originally formulated. The KL scheme calculates the changes in the sub-grid scale variation of RHi in a cloud parcel as a result of updrafts or downdrafts and the growth or decay of ice particles. Unlike some schemes (e.g. Shi et al., 2015) which consider that the initial nucleation in an updraft takes place in the presence of ice from the previous time step, we assume the first parcel updraft within a GCM time step does not carry any preexisting ice, but thereafter if ice forms it may either grow and decrease the supersaturation or evaporate adding water vapor to the parcel. However, aerosols freeze in the order of size bins and this neglects the competition among different aerosol size bins, which results in an underestimation of the ice formed from aerosols in small size bins and a low sensitivity to the change of aerosol number

226   (Liu and Shi, 2018). In this study, we combined the LP and KL parameterizations to
227   develop a new ice nucleation scheme (hereafter HYBRID) to make use of their
228   strengths and avoid their defects.

229   In the HYBRID scheme, the supersaturation (S_i) in the cloud parcel is
230   calculated explicitly using the KL scheme so that ice particles are able to grow or
231   decay throughout the time variations in the updrafts and downdrafts associated with
232   gravity waves. S_i is calculated as a function of the updraft and aerosol concentrations
233   at each grid. S_i is updated every second using

$$234 \qquad \frac{dS_i}{dt} = a_1 S_i w - (a_2 + a_3 S_i) \int_0^\infty dr_0 \frac{dn}{dr_0} R_{im}(r_0)$$

235   where the parameter a_1 is given by $a_1 = (L_s M_w g)/(c_p R T^2) - Mg/(RT)$, with the
236   molar mass of air M and water M_w, latent heat of sublimation L_s, constant of gravity
237   g, heat capacity at constant pressure c_p, the universal gas constant R, and air
238   temperature T. w is the vertical velocity. $a_2 = 1/n_{sat}$ with the water vapor number
239   density at ice saturation n_{sat}. $a_3 = L_s^2 M_w m_w/(c_p p T M)$, with the mass of a water
240   molecule m_w and the air pressure p. R_{im} is the monodisperse freezing/growth integral,

$$241 \qquad R_{im} = \frac{4\pi}{v} \int_{-\infty}^t dt_0 \dot{n}_i(t_0) r_i^2(t_0, t) \frac{dr_i}{dt}(t_0, t),$$

242   where v is the specific volume of a water molecule. $dt_0 \dot{n}_i(t_0)$ is the number density
243   of aerosol particles that nucleate ice and freeze within the time interval between t_0
244   and $t_0 + dt_0$, $r_i(t_0, t)$ is the radius of the spherical ice particle at time t that froze
245   and commenced to grow at time $t < t_0$, and dr_i/dt is the radial growth rate of that
246   ice particle. In the HYBRID scheme, $\dot{n}_i(t_0)$ is determined using the LP
247   parameterization.

248   A series of updraft velocities at each grid point was generated based on a fitted
249   wave spectrum to the observed equatorial gravity waves from Podglajen et al. (2016).
250   The standard deviation of this wave spectrum was extended to other latitudes and

251   seasons by using the parameterization proposed by Gary (2006, 2008). It was

252   extended vertically based on the static stability, atmospheric density and topography.

253   This parameterization of the wave spectrum associated with gravity waves is

254   described in Penner et al. (2018).

255   When the updraft velocity is positive, the LP parameterization is used to

256   calculate the increase in the ice number from homogeneous and/or heterogeneous

257   freezing, so that the HYBRID scheme avoids the lack of sensitivity to changes in

258   aerosol number in the KL parameterization when calculating the number of new ice

259   particles. The LP parameterization is derived by fitting the results of a large set of

260   parcel model simulations covering different conditions in the upper troposphere (Liu

261   and Penner, 2005). Two separate regimes are identified by the sign of $T -$

262   $6.07 \ln w + 55.0$ (where T is the temperature and w is the updraft velocity) to

263   calculate the change of Ni due to homogeneous nucleation. When the sign is positive,

264   the solution is in fast-growth regime which is associated with higher T and lower w.

265   The number concentration of new ice crystals (N_i or $\dot{n}_i(t_0)$ as in the above) is then

266   calculated with the following equation

267   $$N_i = min\{exp(a_2)N_a^{a_1}exp(bT)w^c, N_a\}$$

268   where $b = b_1 lnN_a + b_2$, and $c = c_1 lnN_a + c_2$. N_a is the number concentration of

269   sulfate in the Aiken and accumulation modes. The coefficients a_1, a_2, b_1, b_2, b_3, c_1,

270   c_2 are constant, and can be found in Table 1 of Liu and Penner (2005). For lower T

271   and higher w (the slow-growth regime), the following equation is applied to calculate

272   N_i:

273   $$N_i = min\{exp[a_2 + (b_2 + b_3 lnw)T + c_2 lnw]N_a^{a_1+b_1T+c_1 lnw}, N_a\}$$

274   where the coefficients a_1, a_2, a_3, b_1, b_2, b_3, c_1, c_2 are again listed in Table 1 of Liu

275   and Penner (2005) and are different from those in the fast-growth regime. The

276 number concentration of N_i from INPs in the heterogeneous nucleation regime is

277 given as

278 $$N_i = min\{exp(a_{22})N_{INP}^{b_{22}}exp(bT)w^c, N_{INP}\}$$

279 where $b = (a_{11} + b_{11}lnN_{INP})lnw + (a_{12} + b_{12}lnN_{INP})$ and $c = a_{21} + b_{21}lnN_{INP}$.

280 N_{INP} is the number concentration of total INPs. The coefficients a_{11}, a_{12}, a_{21}, a_{22}, b_{11},

281 b_{12}, b_{21}, b_{22} can be found in the Section 4.2 of Liu and Penner (2005). When the

282 updraft velocity is low and temperature is high, heterogeneous ice nucleation takes

283 place initially and depletes the water vapor in the parcel so that homogeneous ice

284 freezing never occurs. The threshold temperature T_c for heterogeneous nucleation-

285 only is given by

286 $$T_c > aln(w) + b$$

287 where $a = -1.4938ln(N_{INP}) + 12.884; b = -10.41ln(N_{INP}) - 67.69$. When the

288 regime is in a transition from heterogeneous-dominated to the homogeneous-

289 dominated regimes, the total ice number concentration from nucleation can be higher

290 than the ice concentration from only heterogeneous nucleation, but lower than that

291 from the pure homogeneous nucleation case. Then, N_i is interpolated from

292 $$N_i = N_{Het}\left(\frac{N_{Het}}{N_{Hom}}\right)^{\frac{N_{INP}-N_c}{0.9N_c}}$$

293 where N_{Het} is the ice number from pure heterogeneous nucleation, N_{Hom} is the ice

294 number from pure homogeneous nucleation, N_{INP} is the number concentration of

295 INPs and N_c is the critical number concentration of INPs for the heterogeneous

296 nucleation-only regime.

297 Based on the method outlined above, HYBRID scheme calculates the increase

298 in Ni using LP parameterization. The new ice crystals from nucleation either grow

299 or decay with consumption/evaporation of water vapor and therefore change Si,

300   which is determined using KL parameterization. The changes in *Si* then influence

301   which particles are able to nucleate forming ice crystals.

302   We define cirrus clouds for which the effects of aerosols are defined/calculated

303   as all large-scale clouds formed at temperatures < -35°C. Cirrus clouds at these

304   temperatures include anvil cirrus that are formed by the outflow from deep

305   convection as well as large-scale cirrus formed by in-situ gravity waves. The

306   detrained ice crystal number concentration in anvils is calculated from the detrained

307   ice mass by assuming a spherical particle with a constant volume-mean radius,

308   which is approximated as $3\rho_0 Q/(4\pi\rho_i r_{iv}^3)$ following Lohmann (2002). ρ_i is the ice

309   crystal density, ρ_0 is the air density, r_{iv} is the volume mean radius determined from

310   a temperature-dependent lookup table (Kristjánsson et al. 2000; Boville et al. 2006),

311   Q is the detrainment rate of cloud water mass diagnosed from the convection

312   parameterization. The new clouds generated by convective detrainment are assumed

313   to be at saturation with respect to ice. In doing this, anvil clouds and in situ cirrus

314   compete for the available water vapor within a grid box. When anvil clouds are

315   formed due to convective detrainment, it reduces the saturation ratio in the clear-sky

316   portion of a grid, and can potentially reduce the frequency of in situ large-scale cirrus

317   formation (Wang and Penner 2010; Wang et al. 2014). We only calculate *Ni* as a

318   result of the nucleation of aerosol in large-scale cirrus, so that when anvils occur in

319   a grid box, we average the concentrations to determine the total ice number

320   concentration in cirrus clouds. Anthropogenic emissions contribute to the change in

321   the number concentration of ice crystals in large-scale cirrus cloud, but these are

322   then averaged with the crystals in anvils.

323

324   2.2.1 Evaluation of the HYBRID scheme

325   In order to examine the ability of the HYBRID ice nucleation scheme to

326   simulate ice number concentration, the results from a box model using the HYBRID

scheme are compared with those from an adiabatic parcel model under the same simulation conditions. The adiabatic parcel model was that used to generate the LP parameterization and was introduced in Liu and Penner (2005). The two models are run for 30 min for each simulation, which is the time step used in the CESM. During the 30 min, the updraft velocity is updated every 2.2 min as recommended by Podglajen et al. (2016). The ice number concentrations after the 30 min simulation from the two models are compared. We ran both the adiabatic parcel model and the HYBRID box model using a constant updraft velocity for each 2.2-min interval. When the velocity is positive ice crystals form and grow in the HYBRID box model as described above. For downdrafts, if the supersaturation is below 100%, the two models use the same method to simulate the evaporation of any existing ice particles, which is also the same method used in the global model as suggested in Kärcher et al. (2006). The scheme used here for the HYBRID box model is the same as the HYBRID scheme used in the global model. Note that the final interval within each 30 minute simulation is shortened in order to match the treatment used in the CESM/IMPACT model which uses a 30 minute time step. When run within the CESM model, this final ice number concentration is then passed back to the CESM model after this 30 minute interval.

The updrafts and downdrafts associated gravity waves are determined from a Laplace distribution as suggested by the fit to the observed gravity waves by Podglajen et al. (2016). We conducted 10,000 simulations using a random selection of the updrafts and downdrafts for each model. Both models use the same selection of updrafts and downdrafts in each simulation. We set up an initial condition with a temperature of 230K, the standard deviation for the updraft velocities was 0.5 m s^{-1} and the initial RHi was 130%. The sulfate number concentration was set to 0.2 L^{-1}

while the dust concentration was 10 L^{-1}. These particles then participate in either homogeneous nucleation or heterogeneous immersion nucleation.

Figure 1 shows a histogram of the predicted ice number concentration (Ni) for 10,000 simulations of the adiabatic parcel model and the box model using the HYBRID scheme. Two populations of Ni are shown in Figure 1. The lower population (with concentrations of the order of 10 L^{-1} or less) represents primarily heterogeneous nucleation on dust particles, while the higher population (with concentrations of the order of 10^2 L^{-1} or more) represents primarily homogeneous nucleation on sulfate aerosols. The results in the simulations dominated by heterogeneous nucleation are mostly similar for the two models, although the HYBRID scheme overestimates the Ni between 1~10 L^{-1} when the results from the adiabatic parcel model are less than 10^{-1} L^{-1} for some of these same simulations. The average Ni from heterogeneous nucleation over 10,000 simulations from the adiabatic parcel model is 9.40±2.31 L^{-1}, while that from the HYBRID scheme is 9.52±2.08 L^{-1}.

The box model using the HYBRID scheme predicts larger Ni from homogeneous nucleation than the parcel model in the 88% of simulations where homogeneous nucleation occurs. There are more simulations using the HYBRID scheme that predict larger Ni from homogeneous nucleation than the parcel model as indicated by larger number of counts of large Ni (10^4 L^{-1} or more) in Figure 1. The HYBRID scheme uses the LP parameterization for every small time step of 2.2 min. Since the LP parameterization was built using the largest Ni in an ascending parcel after 30 min, there is a tendency for the HYBRID scheme to overpredict Ni. The average Ni from homogeneous nucleation over the 10,000 simulations in the two models is 1.41±4.23 L^{-1} from the parcel model, while it is 1.52±4.83 L^{-1} from the HYBRID model. The HYBRID scheme overestimates the Ni from homogeneous

nucleation by 7.4%, which dominates the difference in total Ni between two models. Overall, the average total Ni over the 10,000 simulations is 1.53 ± 4.83 L^{-1} using the HYBRID scheme, which is 7.3% larger than the result from the parcel model (1.42 ± 4.23 L^{-1}). We also examined the difference between the above case when sulfate was 200 cm^{-3} compared to when sulfate was 20 cm^{-3}, and the difference was within 7.2% of that using the full parcel model. Although the HYBRID scheme predicts a somewhat larger number of nucleated ice particles, on average, the results are reasonable compared to the results from the parcel model.

2.3 Experiments with the global model

We performed a series of model experiments in which different emissions of aerosols and aerosol precursors are used. Table 2 provides a summary of these experiments. The base case (PD_Base) uses emissions for the present day (PD, for the year 2000) for anthropogenic sulfur and soot from fossil fuel adopted from Community Emission Data System (CEDS) (Hoesly et al., 2018). Emissions from van Marle et al. (2017) are adopted for biomass burning emissions. These emissions are the same as the emissions datasets used for the CMIP6 simulations. The year 2000 emissions are used for all years of our simulation. We included soot from aircraft for 2006 based on the Aviation Environment Design Tool (AEDT) data set (Barrett et al., 2010). The AEDT data are presumed to be more accurate than the CMIP6 aircraft emissions since they were developed based on the original flight tracks of each of 31 million commercial flights worldwide (Wilkerson et al., 2010). The dimethylsulfide (DMS) emissions from the ocean are assumed constant in the PD and PI periods (Tilmes et al., 2016). The emission of dust uses the scheme from Zender et al. (2003). In a sensitivity experiment (PI_cSoot), the emission of cSoot is

404 removed from PD_Base to examine its impact on ice number concentration and
405 radiative forcing. We also set a case (PI_SO4) with the emission of anthropogenic
406 sulfur changed to PI ($\approx$1750) to calculate the radiative forcing of sulfur. The case
407 PI_ALL set all emissions to those of the PI period ($\approx$1750) to examine the radiative
408 forcing of all anthropogenic aerosols on cirrus cloud. Additionally, we set up two
409 experiments to examine the effect of SOA as an INP on anthropogenic forcing in
410 cirrus clouds. The case PD_SOA and PI_SOA adds newly nucleated SOA particles
411 that have grown to the accumulation mode as additional INPs to the cases of
412 PD_Base and PI_ALL. The cases including SOA in the PD and PI read in the explicit
413 number concentration of newly formed SOA in the accumulation mode nucleated
414 from highly oxygenated organic molecules (HOMs) that form from the oxidation of
415 α-pinene. The nucleated SOA particles grow by deposition and coagulation of
416 sulfuric acid as well as the oxidation products of isoprene, α-pinene, limonene and
417 aromatics, that are in the aerosol phase. This SOA was simulated using the version
418 of the CESM/IMPACT model outlined in Zhu et al. (2017, 2019) and Zhu and
419 Penner (2019, 2020). The SOA that meets the requirements of the glass transition
420 temperature and RHi calculated using the equations in Wang et al. (2012) acts as an
421 effective heterogeneous INP.

422   The changes in aerosol emissions only influence the number concentration of
423 ice nuclei in the CESM, and thereby give the indirect radiative effect in cirrus clouds.
424 The direct radiative effect caused by the change of aerosols is not included. Clear
425 sky radiative forcing in this study is not associated with direct aerosol radiative
426 forcing, but is rather mainly due to changes in water vapor which leads to changes
427 in the clear sky longwave radiation (Wang and Penner, 2010). All cases were run
428 with prescribed sea surface temperatures for the present day and winds were nudged
429 towards ECMWF reanalysis data for the years 2005-2011 using a nudging time of 6

430   hours (Zhang et al., 2014). The data for the last six years were used for analysis in

431   this study.

432

3. Results from the global model

3.1 Ice number concentrations

435   The predicted Ni in PD_Base case is compared with the observed Ni reported

436   by Krämer et al. (2009) and Krämer et al. (2020) in Figure S1. Data from the model

437   have been selected to have ice water mixing ratios $> 10^{-8}$ kg kg^{-1} to match values

438   seen in the in-situ observations (Krämer et al., 2016). The global model using the

439   HYBRID scheme is able to do a reasonable job in predicting Ni with the difference

440   in the median value between the simulation and observation less than 50% for all

441   temperatures except for the high concentrations seen between 197K and 213K. The

442   model predicts ~3 times higher *Ni* on average compared to the observations

443   between 197K and 213K. Although the comparison of ice number concentration

444   between our model and observation has not improved significantly compared to

445   that shown by Penner et al. (2018), the new nucleation scheme improves the ability

446   of nucleation to occur on small sized particles, since it avoids the calculation of ice

447   nucleation chronologically from large sizes to small size used in the KL scheme,

448   which results in an underestimation of ice crystals formed from small size particles.

449   The global average *Ni* in the PD_Base is 0.15×10^{10} m^{-2} with the largest *Ni* in

450   the tropics of Eastern Hemisphere (Figure 2a). Most ice particles nucleate in the

451   upper troposphere (150~200 hPa) in the tropics, while some ice nucleation occurs

452   in the lower troposphere (around 300 hPa) in the polar regions (Figure 2b). The ice

453   particles formed from homogeneous nucleation dominate the total *Ni* in most

454   regions over the world (Figure S2a) and are responsible for ~95% of global average

Ni (Figure 2c). The large number concentration of sulfate in the Aitken and accumulation modes in the upper troposphere over the west Pacific Ocean and north Indian Ocean contributes to the remarkably large Ni in the tropical Eastern Hemisphere. Heterogeneous nucleation dominates the Ni in the northern middle-high latitudes where anthropogenic soot emission is high (Figure S2a), although the Ni from heterogeneous nucleation is high in the tropics (Figure 2e). Homogeneous nucleation mostly occurs in the upper troposphere (around 200hPa in the tropics and around 300hPa in the extratropical regions), while heterogeneous nucleation is an important contributor to Ni in the middle and lower troposphere (Figure S2b). Although the Ni from homogeneous nucleation is high, the occurrence frequency of homogeneous nucleation (calculated as the ratio of the time steps when homogeneous nucleation occurs to all time steps with nucleation occurring) is up to ~20% in the tropics and < 5% in most other regions (Figure S2c). Due to the lack of the effect of orographic wave on ice nucleation, the observed increases in ice number over orography, particularly over the Andes, Rockies, the Antarctic mountains, and Greenland are not shown in Figure 2.

The competition between the heterogeneous INPs and homogeneous haze particles determines the change in Ni between the PD and PI periods. We set up three sensitivity cases to separately examine the effects of the emission of cSoot for aircraft, anthropogenic sulfur and all anthropogenic emissions on Ni. INPs always nucleate prior to homogeneous nucleation in a rising air parcel, so they consume the available water vapor and inhibit homogeneous freezing when added to regions dominated by homogeneous nucleation. The Ni formed from heterogeneous nucleation increases significantly around 200hPa over the world due to the inclusion of INPs from cSoot, especially near Southeast Asia (Figure 3e, 3f). Simultaneously, homogeneous nucleation is inhibited significantly around 200hPa in Southeast Asia and other tropical regions (Figure 3c, 3d). The emissions of aircraft soot that form

contrails peak near 200hPa with the spatial distribution shown in Figure 1a in the Zhou and Penner (2014). Although the emissions of aircraft soot are large in midlatitude, the effect of inhibiting homogeneous nucleation as a result of adding the heterogeneous nucleation is large in the tropics (Figure 3c). That is because of the largest number concentration of ice nuclei from homogeneous nucleation in the tropics as shown in Figure 2c. Due to the much larger decrease in Ni from homogeneous nucleation than the increase in Ni from heterogeneous nucleation, the global average Ni is decreased by 0.1×10^8 m^{-2} (1%) when including the emission of aircraft soot (Figure 3a). The change in Ni due to cSoot is small with a significant change only over the North Atlantic Ocean and east coastal regions in North America (Figure 3a).

In contrast to the case of aircraft soot, the increase in the sulfur emissions from PI to PD leads to a large increase in Ni from homogeneous nucleation in most regions, which causes an increase of 1.01×10^8 m^{-2} in the global average Ni (Figure 4c). The increase in Ni from homogeneous nucleation contributes to the significant increase in Ni near 150hPa over South Asia, Africa and the North Indian Ocean (Figure 4a). The decrease in Ni from heterogeneous nucleation offsets some of the increase in Ni from homogeneous nucleation and leads to a significant decrease in Ni near 300hPa over the North Pacific Ocean (Figure 4a). In total, the global average Ni is increased by 0.73×10^8 m^{-2} (5%) due to the increase in sulfur emissions.

The change in Ni from PI to PD due to all anthropogenic emissions is a balance among the effects of increasing INPs from surface emissions and aircraft soot as well as the increase in haze particles. The effect of all anthropogenic emissions on Ni is mostly dominated by the increase in Ni from homogeneous nucleation caused by the increase in sulfur emissions, but homogeneous nucleation is inhibited somewhat by increased INPs from soot (compare Figure 5c and 4c). As a result, the

508   global average increase in *Ni* from homogeneous nucleation between PD_Base and

509   PI_ALL is only 58% of that between PD_Base and PI_SO4. The change in *Ni* from

510   heterogeneous nucleation is decreased in the mid-high latitudes of the Northern

511   Hemisphere (NH) from PD_Base to PI_ALL similar to the decrease from PD_Base

512   to PI_SO4 (Figure 5e, 5f). However, the increase in INPs from soot near Southeast

513   Asia leads to a small increase in *Ni* from heterogeneous nucleation there (Figure 5e).

514   In total, the increase in all anthropogenic emissions causes a significant increase of

515   *Ni* in South Asia and the North Indian Ocean while a significant decrease of *Ni* is

516   found in mid-latitude regions and some Arctic regions, resulting in $0.49 \times 10^8 \, \text{m}^{-2}$ (3%)

517   more *Ni* from PI to PD for the global average.

518   It is conspicuous that sulfur and aircraft soot emissions have effects with different

519   signs for the change in *Ni* (Figure 3a, 4a). Generally, INPs from aircraft soot

520   decrease *Ni* due to the suppression of homogeneous nucleation in the regions

521   dominated by homogeneous nucleation, while the increase in sulfur emissions

522   increases *Ni* in these same regions due to the enhancement of homogeneous

523   nucleation. However, the changes to *Ni* have opposite signs in the west Pacific Ocean

524   off the coast of Southeast Asia, where the homogeneous nucleation is most active

525   (Figure 2c). We attribute this to the possible effect of aerosol and cloud feedbacks

526   to the meteorological state. When including aircraft soot, the temperature is

527   decreased (Figure S3b) and the RHi is increased (Figure S3a) around 150hPa over

528   the west Pacific Ocean, where *Ni* from homogeneous nucleation increases a lot

529   (Figure 3c). The decrease in temperature is beneficial to homogeneous nucleation.

530   Meanwhile, the emission of aircraft soot is very low in the west Pacific Ocean due

531   to the lack of flight routes there (refer to Figure 1a in Zhou and Penner (2014)), so

532   that the effect of aircraft soot on the suppression of homogeneous nucleation is weak

533   in that region (Figure 3e). As a result, the *Ni* from homogeneous nucleation is

534   increased, which determines the increase in the Ni near 150 hPa over the west Pacific
535   Ocean due to the emission of aircraft soot (Figure 3a). Similarly, when the sulfur
536   emissions are increased from PI to PD, the change in cirrus clouds influences the
537   meteorological state. A large decrease in RHi at 150hPa is found in the west Pacific
538   Ocean (Figure S4a), so that the occurrence frequency of homogeneous nucleation
539   decreases when sulfur emissions increase (Figure S4d). Additionally, the
540   temperature at 150hPa increases over the world (Figure S4b), which also contributes
541   partly to the decrease in the occurrence frequency of homogeneous nucleation.
542   Although global sulfur emissions increase sharply from PI (2.2 Tg S year^{-1}) to PD
543   (55 Tg S year^{-1}), the anthropogenic emissions mainly occur on the mainland with
544   much smaller emissions over the ocean even though the sulfur emissions from
545   shipping increase by 6.4 Tg S year^{-1}. The column number concentration of sulfate
546   having the potential to freeze homogeneously do not increase significantly over most
547   ocean regions (Figure S4c), so that the decrease in the occurrence frequency of
548   homogeneous nucleation leads to a decrease in Ni from homogeneous nucleation
549   over the west Pacific Ocean (Figure 4c). The increase in the temperature in the upper
550   troposphere over the world (Figure S4b) also partly explains the decrease in Ni from
551   heterogeneous nucleation when only sulfur emissions increase (Figure 4e). The
552   feedbacks to the meteorological state in remote regions always have an opposite
553   effect on the changes in Ni compared to the effect in regions with large
554   anthropogenic emissions. These meteorological feedbacks partly reduce the changes
555   in global average Ni due to anthropogenic emissions. Although these opposite
556   changes in Ni due to meteorological feedbacks are not statistically significant
557   (Figure 3a, 4a, 5a), our conjecture based on the model results indicates that the
558   meteorological feedbacks caused by the radiative effects of aerosols might
559   contribute to the change in Ni in remote regions. These important feedback processes
560   need to be investigated further.

561

3.2 Radiative forcing

The decrease in Ni in the upper troposphere usually leads to an increase in the size of ice particles, which promotes the gravitational removal and formation of snow, causing a decrease in the ice water path (IWP) and vice versa. As a result, the change in IWP is mainly determined by the change in Ni and have a similar geographic pattern. The global average IWP in the model is 14.6 g m^{-2} for the PD_Base case, which is lower than that observed in different CloudSat/CALIPSO analyses (21~28 g m^{-2}) (*Li et al.*, 2012). We used a cut off diameter of 250 μm to move cloud ice to snow. A cutoff diameter of 400 μm in the model almost doubles the IWP in our model (compare IWP of dbfc_mg10 and dbfc in Table 3 in Penner et al., 2018). The emission of aircraft soot leads to a significant decrease in IWP in Southeast Asia and the East coast of North America, caused by the inhibition of homogeneous nucleation (Figure 6a). As shown in Figure 6b, the increase in the sulfur emissions leads to a significant increase in IWP in the north Indian Ocean due to the changes in Ni from homogeneous nucleation. The decrease in IWP in East Asia and the Arctic is attributed to the decrease in Ni from heterogeneous nucleation (Figure 6b). The geographic pattern of changes in IWP due to the change in all anthropogenic emissions from PI to PD is dominated by the changes in IWP caused by the changes in sulfur emissions (compare Figure 6b and 6c). However, the increase in IWP in tropical regions is smaller and the decrease in IWP in the middle and high latitudes of the NH is more negative in the PD_Base-PI_ALL case compared to the PD_Base-PI_SO4 case because of the inhibition of homogeneous nucleation caused by the increase in the emission of surface and aircraft soot. As a result, although the geographical pattern of the changes in IWP is similar for the

586   PD_Base-PI_ALL and PD_Base-PI_SO4 cases, the magnitude of changes in the

587   global average IWP switches from positive (0.07 g m^{-2} for PD_Base-PI_SO4, Figure

588   6b) to negative (-0.13 g m^{-2} for PD_Base-PI_ALL, Figure 6c).

589   The changes in Ni and IWP lead to a change in the cirrus cloud fraction and also

590   feedback to produce a change in the lapse rate of temperature, which has an effect

591   on the delivery of water vapor and the strength of convection and these changes

592   influence the formation and lifetime of liquid water clouds. The liquid water path

593   (LWP) changes due to these complex dynamical feedbacks are shown in Figure S5.

594   The changes in global average LWP are all less than 0.5% with only a small number

595   of grids with a significant change. The changes in the shortwave and longwave

596   radiative fluxes are determined by the changes in LWP and IWP (as well as the

597   change in Ni), although they are dominated by the change in IWP. The changes in

598   aerosol only have a direct effect on the cirrus clouds in our model, while the changes

599   in warm clouds are caused by feedbacks due to the change in cirrus clouds. The

600   changes in the all-sky shortwave radiative forcing (SRF) and longwave radiative

601   forcing (LRF) at the top of the atmosphere (TOA) generally follow the changes in

602   IWP but have the opposite sign (Figure 7, Figure 8 and Figure 9). The changes in

603   LWP could either enhance or offset the effect of changes in IWP on the radiative

604   fluxes depending on whether the sign of the changes in IWP and LWP are

605   reinforcing or not. The emission of cSoot leads to a positive global average SRF due

606   to the significant increase in shortwave radiative fluxes off the coast of East Asia

607   and over the North Indian Ocean, while and the significant decrease in the longwave

608   radiative fluxes over East Asia, the North Indian Ocean and North Atlantic Ocean

609   contribute to a negative global average LRF mostly due to the decrease in the global

610   average IWP (Figure 7). On the other hand, the increase in sulfur emissions causes

611   a negative global average SRF largely due to the significant decrease over South

Asia, North Africa and the North Indian Ocean (Figure 8a). Simultaneously, the increase in the IWP in these regions leads to a significant increase in longwave radiative fluxes resulting in a positive global average LRF, although the LRF is significantly negative in the middle to high latitude over the east coast of Asia. (Figure 8b). The changes in the SRF and LRF due to the increase in all anthropogenic emissions have a similar geographic pattern to those caused by the increase in sulfur emissions but the global average forcings have opposite signs (compare Figure 8c, 8d and Figure 9c, 9d). This is due to the decrease in the global average IWP caused by the inhibition of homogeneous nucleation as a result of the increased emissions of soot.

The total all-sky net forcing (NRF) is determined by the balance between SRF and LRF. The radiative effects in cirrus clouds are dominated by longwave radiative effects. However, it is still possible that the radiative forcing due to changes in Ni in cirrus clouds in some regions is dominated by SRF due to the combined effects on shortwave forcing from the changes in cirrus clouds together with changes to warm clouds caused by feedbacks. The emission of cSoot has a negative global average NRF of -0.14 ± 0.07 W m^{-2} in cirrus clouds with only a few significant grids, although the SRF and LRF due to cSoot are significant in some coastal regions off of East and South Asia (Figure 7). The NRF due to cSoot is most negative around the 30°N where the emission of aircraft soot is high, while there is a small positive forcing around 10°N dominated by SRF (Figure 7f). The NRF is the sum of the clear sky net radiative forcing (NRFC) and the cloud radiative forcing (CRF) caused by changes in cSoot. The global average CRF is -0.10 ± 0.07 W m^{-2}, which dominates over the NRFC and explains 72% of the NRF of cSoot (Figure 7c, 7d).

Although the increase in sulfur emissions from PI to PD leads to an increase in the global average Ni and IWP, the global average NRF due to sulfur emissions is

near zero, -0.02 ± 0.06 W m^{-2}. The NRF due to sulfur emissions is significant and positive (up to 7.1 W m^{-2}) around the 30°N in South Asia and North Africa (Figure 8e). The NRF is negative over most mid to high latitudes of the NH, which is attributed to the decrease in LRF associated with the feedback to the decrease in Ni from heterogeneous nucleation there. However, the significant negative NRF in the north Indian Ocean and positive NRF in the west Pacific Ocean are dominated by the change in SRF (Figure 8a, 8e). The LWP increases in the north Indian Ocean as a result of dynamic feedbacks from the changes in the cirrus clouds, leads to the significant SRF together with the changes in IWP and cirrus clouds. The negative NRF in the north Indian Ocean and mid to high latitudes of the NH offset the positive NRF around the 30°N (Figure 8e). The significant negative NRF over the North Indian Ocean is dominated by the CRF, while the significant positive NRF over South Asia and North Africa is the combined effect of CRF and NRFC. The global average CRF is -0.17 ± 0.06 W m^{-2} and determines the sign of the global average NRF. However, the global average NRFC is 0.14 ± 0.02 W m^{-2} with a wide area of positive values over the NH, which offsets most of CRF.

Compared to the NRF due to the increased sulfur emissions, the NRF is less positive in South Asia and more negative over the mid to high latitudes of the NH and the north Indian Ocean when including the increased emissions of surface and aircraft soot as well as sulfur together (Figure 9e). In the mid to high latitudes of the Southern Hemisphere (SH), SRF and LRF always cancel each other so that NRF is negligible. As a result, the global average NRF due to the all increased anthropogenic emissions from PI to PD is -0.20 ± 0.05 W m^{-2}, which is mainly dominated by the changes in LRF (Figure 9e, 9f). Both the CRF and NRFC due to all anthropogenic emissions are largely explained by the CRF and NRFC caused by change in emission of sulfur (compare Figure 9c, 9d and Figure 8c, 8d). The global average CRF is -

664   0.28 ± 0.04 W m^{-2} due to the changes in all anthropogenic emissions, while the NRFC

665   is slightly positive (0.08 ± 0.02 W m^{-2}).

666

3.3 The influence of SOA on anthropogenic forcing

668   SOA particles have a strong potential to act as INPs and therefore influence the

669   formation of cirrus clouds. We examined the radiative forcing of all anthropogenic

670   aerosols on cirrus clouds when including the INPs from newly-nucleated SOA

671   particles. Figure 10 shows the column number concentration of INPs and zonal

672   average of INPs from SOA in the PD and PI atmosphere. Changes in natural SOA

673   precursors between the PI and PD atmospheres (i.e. isoprene, α-pinene and

674   limonene emissions) are caused by changes in temperature as well as by changes in

675   land-use, while changes in aromatic emissions are associated with anthropogenic

676   emission growth. In addition, newly formed SOA particles grow to accumulation

677   mode size as a result of coagulation of particles (sulfate and other newly formed

678   SOA particles), deposition of gaseous sulfate and incorporation of other SOA

679   compounds (e.g. through partitioning or kinetic uptake). Thus, the number

680   concentration of INPs from SOA is much higher in the PD than that in the PI due to

681   the much higher concentration of SOA in the accumulation mode in the PD (Zhu et

682   al., 2019). The INPs from SOA are highest in the middle latitude of the NH in the

683   PD, while the INPs from SOA are higher in the SH than that in the NH in the PI

684   atmosphere (Figure 10a, 10b). The INPs from SOA in the PD are spread between

685   600hPa to 150hPa with a peak around 300hPa, so there is a possible influence on the

686   formation of cirrus clouds (Figure 10b). The INPs from SOA in the PI have a peak

687   concentration that is a little higher than those in the PD (Figure 10d). The global

688   average Ni from heterogeneous nucleation increases by 1.86×10^8 m^{-2} from PI to PD

when including the INPs from SOA (Figure 11e), which is in contrast to the decrease in the global average Ni from heterogeneous nucleation in the case without SOA (Figure 5e). The INPs from SOA increase the Ni from heterogeneous nucleation in both the PD and PI cases when compared to the PD_Base and PI_ALL cases (Figure S6e, Figure S7e). However, the increase in Ni from heterogeneous nucleation in the PD is much larger than that in the PI because of the larger number concentration of INPs from SOA in the PD. As a result, the large increase in INPs from SOA between the PD and the PI enhances heterogeneous nucleation resulting in an increase in Ni from heterogeneous nucleation especially in the tropics around 150hPa and in Antarctic from 400hPa to 200hPa (Figure 11f). The increase in the heterogeneous nucleation when including SOA widely inhibits homogeneous nucleation in both the PD and PI (Figure S6c, Figure S7c). In the PD, the increase in Ni from heterogeneous nucleation even outweighs the decrease in Ni from homogeneous nucleation leading to an increase of 0.4×10^8 m^{-2} in the global average Ni due to SOA compared to the PD_Base case (Figure S6a). In contrast, the INPs from SOA in the PI case make a larger contribution to the decrease in Ni from homogeneous nucleation than the increase in Ni from heterogeneous nucleation resulting in a decrease in total Ni of -0.31×10^8 m^{-2} compared to the PI_ALL case (Figure S7a). The inclusion of INPs from SOA decreases Ni in the tropics but increases Ni in the mid to high latitudes in both the NH and SH (Figure S6b, S7b). The global average Ni in the PD increases while the global average Ni in the PI is decreased. Both changes are caused by additional INPs from SOA (Figure S6a, S7a) resulting in a larger increase in the global average Ni from the PI to PD compared to the case without SOA (compare Figure 5a and Figure 11a). When including INPs from SOA, Ni increases to a large extent over south Asia, the north Indian Ocean and Antarctica due to the increase in heterogeneous nucleation, while Ni decreases over the mid to high latitude of East Asia and the North Pacific Ocean (compare Figure 11a and Figure 5a).

716   The increased Ni leads to a significant increase in the IWP in south Asia, the

717   north Indian Ocean and Antarctica due to the reduction of gravitational removal,

718   while the IWP decreases significantly in the mid to high latitude of East Asia which

719   is caused by the decrease in Ni (Figure 11a). Compared with the case without SOA

720   (PD_Base-PI_ALL), the inclusion of SOA increases the difference in the IWP

721   between the PD and PI in Antarctica significantly because of the increase in Ni from

722   heterogeneous nucleation of INPs from SOA there (Figure 12a). The change in the

723   LWP due to dynamic feedbacks in the case with SOA is significant in only a few

724   grids, which is similar to the case without SOA (Figure 12c). The larger increases in

725   Ni and IWP over South Asia and the north Indian Ocean lead to the larger changes

726   in both SRF and LRF when including SOA compared to the case without SOA, while

727   the significant decrease in Ni in the mid to high latitudes over East Asia leads to a

728   significant decrease in the LRF. The increase in Ni and IWP in Antarctica only

729   increases the LRF but does not change the SRF because of the very low shortwave

730   flux in polar regions (Figure 12c, 12d). The larger decrease in the SRF offsets the

731   increase in the LRF in the tropics when including SOA resulting in a similar value

732   for NRF in the tropics for the cases with and without SOA (Figure 13f). However,

733   the more positive changes in the LRF from PI to PD in Antarctica and the Arctic

734   when including SOA explain the more positive NRF there compared to the case

735   without SOA (Figure 13f). In addition, the NRF in south Asia and north Africa

736   around 30ºN, where NRF is most positive in the case without SOA, becomes even

737   more positive when including SOA due to the larger increases in Ni. As a result, the

738   significant and larger positive NRF over Antarctica as well as south Asia and north

739   Africa around 30ºN cause an increase in the global average NRF due to all

740   anthropogenic aerosol to -0.04±0.08 W m^{-2} when including SOA compared to the

741   value of -0.20±0.05 W m^{-2} in the case without SOA. The NRF when including SOA

742   is up to 6.6 W m^{-2} in the Arabian Peninsula while it is as low as -4.8 W m^{-2} in the

743   north Indian Ocean (Figure 12g). Compared to the case without SOA, the global

744   average CRF is less negative (-0.14±0.07 W m^{-2} compared to -0.28 W m^{-2}) largely

745   due to the significant positive CRF over Antarctica (Figure 12f). Simultaneously,

746   the NRFC is more positive in the case with SOA than the case without SOA, which

747   offset 73% of the CRF (Figure 12e).

748

4. Conclusion and discussion

749

750   This work develops a new ice nucleation parameterization, HYBRID, which is

751   a combination of the LP and KL parameterizations. The global model using this new

752   scheme is able to simulate the growth and decay of ice particles in the updrafts and

753   downdrafts associated with gravity waves as in the modified KL scheme (Penner et

754   al., 2018), and is able to treat the changes in aerosol number concentration from

755   freezing haze particles with fidelity in the sign of the change as in the LP scheme.

756   The HYBRID scheme overcomes some of the deficiencies in previous ice nucleation

757   schemes. We evaluated the HYBRID ice nucleation scheme by comparing the

758   scheme with the Liu and Penner (2005) adiabatic parcel model and by comparing its

759   global predictions using observed Ni. We used 10,000 parcel model simulations to

760   show that the HYBRID box model predicts 7.3% larger Ni than the LP adiabatic

761   parcel model with 21.5% larger Ni from homogeneous nucleation. The global model

762   using the HYBRID scheme overestimates Ni between 195K and 215K somewhat

763   compared to observations, as do earlier simulations with only the KL scheme

764   (Penner et al., 2018). The results of Ni from the HYBRID scheme are in reasonable

765   agreement with observations and thus were used in the CESM/IMPACT global

766   model to estimate the radiative forcing of aerosols in large-scale cirrus clouds. The

767   predicted Ni depends on the competition between homogeneous and heterogeneous

768   nucleation. These two ice nucleation processes dominate the formation of Ni in

different regions and altitudes. The global average Ni is dominated by homogeneous nucleation in the PD atmosphere.

We performed a series of model experiments using the HYBRID ice nucleation scheme to explore the forcing and cloud changes associated with changes in aircraft soot, sulfur emissions and all anthropogenic emissions from the PI to PD. Results are summarized in Table 3. The INPs from aircraft soot usually decrease Ni by the inhibition of homogeneous nucleation in spite of some areas with small increases in Ni. In contrast, the increase in sulfur emissions from PI to PD enhances homogeneous nucleation in most regions and leads to a small decrease in the Ni formed as a result of heterogeneous nucleation. We found that the effect of aerosols in cirrus clouds could feedback to the meteorological state as determined by temperature and RHi, which could have an opposite effect on the changes in Ni due to either aircraft soot or sulfur emissions in the remote regions like the west Pacific Ocean. These meteorological feedbacks partly reduce the changes in the global average Ni due to anthropogenic emissions. The changes in Ni from PI to PD caused by all anthropogenic emissions are dominated by the changes due to the sulfur emissions, but the changes in surface and aircraft soot emission have some effects on the inhibition of homogeneous nucleation.

The changes in Ni due to anthropogenic aerosols lead to changes in IWP as well as LWP due to dynamical feedbacks. The changes in SRF and LRF are always determined by the changes in the IWP (and Ni), but the changes in LWP could either enhance or offset the effects of IWP on the radiative fluxes. Emissions of aircraft soot lead to a positive change in the global average SRF while the global average LRF is negative. The changes in sulfur emissions from the PI to PD atmosphere leads to opposite changes in the global average SRF and LRF compared to aircraft soot because of the different signs of changes in Ni. The total net forcing in cirrus clouds is usually dominated by LRF but it is dominated by SRF when the changes

in warm clouds cause a feedback that reinforces the effect of cirrus clouds on shortwave fluxes. As a result, the emission of aircraft soot has a negative global average NRF of -0.14±0.07 W m^{-2} in large-scale cirrus clouds, while the changes in the sulfur emissions from the PI to the PD lead to a small negative global average NRF of -0.02±0.06 W m^{-2}. The global average NRF due to all anthropogenic emissions from PI to PD, which is estimated to be -0.20±0.05 W m^{-2}, is dominated by the NRF caused by increased sulfur emissions but is more negative than the forcing by sulfur emissions alone due to changes in the emissions of soot.

The influence of SOA on the anthropogenic forcing of aerosols in large-scale cirrus clouds was examined. The additional INPs from SOA increase the Ni from heterogeneous nucleation and decrease Ni from homogeneous nucleation, but the sign of the changes in the total Ni depends on the balance of these two effects. The high number concentration of INPs from SOA in the PD atmosphere causes an increase in Ni compared to not including INPs from SOA while the low number concentration in the PI atmosphere causes a decrease. As a result, the changes in Ni due to the changes in anthropogenic emissions from PI to PD are larger when including INPs from SOA than the case without SOA. The inclusion of SOA mainly increases the changes in the NRF in the polar regions and the regions around 30ºN, resulting in a less negative NRF of -0.04±0.07 W m^{-2} associated with the change in all anthropogenic emissions.

The radiative forcing of anthropogenic aerosols effect on cirrus clouds estimated in this study is less negative than the result indicated in Penner et al. (2009) (-0.38 to -0.56 W m^{-2}) and has a different sign compared with the result shown in Gettelman et al. (2012) (0.27±0.10 W m^{-2}). This is mostly caused by the different treatments for updraft velocity, the concentration of haze particles, and INPs as well as the application of a different ice nucleation scheme. Current models show that homogeneous nucleation dominates the formation of new ice particles in most

regions over the world with the largest contribution to cirrus cloud formation in the tropical upper troposphere (Zhou et al., 2016; Shi and Liu, 2018; Shi et al., 2015). However, some observations indicated the importance and high occurrence frequency of heterogeneous nucleation in the tropical tropopause region (Jensen et al., 2013). Although the inclusion of INPs from newly formed SOA in this study inhibits homogeneous nucleation in the tropics, homogeneous nucleation is still responsible for 75% of total Ni in the PD atmosphere. Laboratory measurements have supported other species acting as INP and enhancing heterogeneous nucleation such as solid ammonium sulfate (Abbatt et al., 2006), which has not been considered in current global climate models. Additional INPs from anthropogenic ammonium sulfate can be expected to increase the anthropogenic forcing in cirrus clouds to be less negative and possibly even positive. The HYBRID ice nucleation scheme overestimates somewhat the ice number concentration produced from homogeneous nucleation compared to a full parcel model. An explicit representation of the ice nucleation process used in the global climate model may be helpful to predict the ice number and therefore radiation budget more correctly in the future. The ability of SOA to act as an INP probably varies depends on the property of different SOA compounds as well as their particle size and mixing state (Baustian et al., 2013; Berkemeier et al., 2014; Charnawskas et al., 2017; Shiraiwa et al., 2017). A global climate model coupled online with the formation mechanism of SOA together with an increased understanding of the ability of SOA to act as an INP would help in estimating the contribution of SOA to ice particle formation more accurately.

Code and data availability

The latest version of CESM/IMPACT model and data used in this study are available from the corresponding authors upon request.

Author contribution

JZ developed the model, performed the simulations, analyzed all data. JP guided the model development and data analysis. Both authors contributed to writing the paper.

Competing interests

The authors declare that they have no conflict of interest.

Acknowledgments

We are grateful to the reviewers and for funding from NSF-GEO grant number 1540954 and National Natural Science Foundation of China (Grant 41625014). Computer time was provided by the NCAR CISL.

References

Abbatt, J., Benz, S., Cziczo, D., Kanji, Z., Lohmann, U., and Möhler, O.: Solid ammonium sulfate aerosols as ice nuclei: A pathway for cirrus cloud formation, Science, 313, 1770-1773, 2006.

Andreae, M. O., Afchine, A., Albrecht, R., Holanda, B. A., Artaxo, P., Barbosa, H. M. J., Borrmann, S., Cecchini, M. A., Costa, A., Dollner, M., Fütterer, D., Järvinen, E., Jurkat, T., Klimach, T., Konemann, T., Knote, C., Krämer, M., Krisna, T., Machado, L. A. T., Mertes, S., Minikin, A., Pöhlker, C., Pöhlker, M. L., Pöschl, U., Rosenfeld, D., Sauer, D., Schlager, H., Schnaiter, M., Schneider, J., Schulz, C., Spanu, A., Sperling, V. B., Voigt, C., Walser, A., Wang, J., Weinzierl, B., Wendisch, M., and Ziereis, H.: Aerosol characteristics and particle production in the upper troposphere over the Amazon Basin, Atmospheric Chemistry and Physics, 18, 921-961, 10.5194/acp-18-921-2018, 2018.

Barahona, D., and Nenes, A.: Parameterization of cirrus cloud formation in large-scale models: Homogeneous nucleation, Journal of Geophysical Research: Atmospheres, 113, 2008.

Barrett, S., Prather, M., Penner, J., Selkirk, H., Balasubramanian, S., Dopelheuer, A., Fleming, G., Gupta, M., Halthore, R., and Hileman, J.: Guidance on the use of AEDT gridded aircraft emissions in atmospheric models, A technical note submitted to the US Federal Aviation Administration, Massachusetts Institute of Technology (MIT), 2010.

Baustian, K. J., Wise, M. E., Jensen, E. J., Schill, G. P., Freedman, M. A., and Tolbert, M. A.: State transformations and ice nucleation in amorphous (semi-)solid organic aerosol, Atmospheric Chemistry and Physics, 13, 5615-5628, 10.5194/acp-13-5615-2013, 2013.

Berkemeier, T., Shiraiwa, M., Pöschl, U., and Koop, T.: Competition between water uptake and ice nucleation by glassy organic aerosol particles, Atmospheric Chemistry and Physics, 14, 12513-12531, 10.5194/acp-14-12513-2014, 2014.

Boville, B. A., P. J. Rasch, J. J. Hack, and J. R. McCaa: Representation of clouds and precipitation processes in the Community Atmosphere Model version 3 (CAM3). J. Climate, 19, 2184–2198, 2006.

Cantrell, W., and Heymsfield, A.: Production of ice in tropospheric clouds: A review, Bulletin of the American Meteorological Society, 86, 795-808, 2005.

Charnawskas, J. C., Alpert, P. A., Lambe, A. T., Berkemeier, T., O'Brien, R. E., Massoli, P., Onasch, T. B., Shiraiwa, M., Moffet, R. C., Gilles, M. K., Davidovits, P., Worsnop, D. R., and Knopf, D. A.: Condensed-phase biogenic-anthropogenic interactions with implications for cold cloud formation, Faraday Discuss, 200, 165-194, 10.1039/c7fd00010c, 2017.

Cziczo, D. J., Murphy, D. M., Hudson, P. K., and Thomson, D. S.: Single particle measurements of the chemical composition of cirrus ice residue during CRYSTAL-FACE, Journal of Geophysical Research-Atmospheres, 109, 10.1029/2003jd004032, 2004.Cziczo, D. J., Froyd, K. D., Hoose, C., Jensen, E. J., Diao, M., Zondlo, M. A., Smith, J. B., Twohy, C. H., and Murphy, D. M.: Clarifying the dominant sources and mechanisms of cirrus cloud formation, Science, 340, 1320-1324, 2013.

DeMott, P., Cziczo, D., Prenni, A., Murphy, D., Kreidenweis, S., Thomson, D., Borys, R., and Rogers, D.: Measurements of the concentration and composition of nuclei for cirrus formation, Proceedings of the National Academy of Sciences, 100, 14655-14660, 2003.

Fan, J., Wang, Y., Rosenfeld, D., and Liu, X.: Review of aerosol–cloud interactions: Mechanisms, significance, and challenges, Journal of the Atmospheric Sciences, 73, 4221-4252, 2016.

Gary, B. L.: Mesoscale temperature fluctuations in the stratosphere, Atmospheric Chemistry and Physics, 6, 4577-4589, 2006.

Gary, B. L.: Mesoscale temperature fluctuations in the Southern Hemisphere stratosphere, Atmospheric Chemistry and Physics, 8, 4677-4681, 2008.

Gettelman, A., Liu, X., Barahona, D., Lohmann, U., and Chen, C.: Climate impacts of ice nucleation, Journal of Geophysical Research: Atmospheres, 117, 10.1029/2012jd017950, 2012.

Gordon, H., Sengupta, K., Rap, A., Duplissy, J., Frege, C., Williamson, C., Heinritzi, M., Simon, M., Yan, C., Almeida, J., Trostl, J., Nieminen, T., Ortega, I. K., Wagner, R., Dunne, E. M., Adamov, A., Amorim, A., Bernhammer, A. K., Bianchi, F., Breitenlechner, M., Brilke, S., Chen, X., Craven, J. S., Dias, A., Ehrhart, S., Fischer, L., Flagan, R. C., Franchin, A., Fuchs, C., Guida, R., Hakala, J., Hoyle, C. R., Jokinen, T., Junninen, H., Kangasluoma, J., Kim, J., Kirkby, J., Krapf, M., Kurten, A., Laaksonen, A., Lehtipalo, K., Makhmutov, V., Mathot, S., Molteni, U., Monks, S. A., Onnela, A., Perakyla, O., Piel, F., Petaja, T., Praplan, A. P., Pringle, K. J., Richards, N. A., Rissanen, M. P., Rondo, L., Sarnela, N., Schobesberger, S., Scott, C. E., Seinfeld, J. H., Sharma, S., Sipila, M., Steiner, G., Stozhkov, Y., Stratmann,

F., Tome, A., Virtanen, A., Vogel, A. L., Wagner, A. C., Wagner, P. E., Weingartner, E., Wimmer, D., Winkler, P. M., Ye, P., Zhang, X., Hansel, A., Dommen, J., Donahue, N. M., Worsnop, D. R., Baltensperger, U., Kulmala, M., Curtius, J., and Carslaw, K. S.: Reduced anthropogenic aerosol radiative forcing caused by biogenic new particle formation, Proc Natl Acad Sci U S A, 113, 12053-12058, 10.1073/pnas.1602360113, 2016.

Hendricks, J., Kärcher, B., and Lohmann, U.: Effects of ice nuclei on cirrus clouds in a global climate model, Journal of Geophysical Research, 116, 10.1029/2010jd015302, 2011.

Hoesly, R. M., Smith, S. J., Feng, L., Klimont, Z., Janssens-Maenhout, G., Pitkanen, T., Seibert, J. J., Vu, L., Andres, R. J., and Bolt, R. M.: Historical (1750–2014) anthropogenic emissions of reactive gases and aerosols from the Community Emissions Data System (CEDS), Geoscientific Model Development (Online), 11, 2018.

Hong, Y., Liu, G. and Li, J. L.: Assessing the radiative effects of global ice clouds based on CloudSat and CALIPSO measurements. Journal of Climate, 29(21), 7651-7674, 2016.

Hoose, C., and Möhler, O.: Heterogeneous ice nucleation on atmospheric aerosols: a review of results from laboratory experiments, Atmospheric Chemistry and Physics, 12, 9817-9854, 10.5194/acp-12-9817-2012, 2012.

Ignatius, K., Kristensen, T. B., Jarvinen, E., Nichman, L., Fuchs, C., Gordon, H., Herenz, P., Hoyle, C. R., Duplissy, J., Garimella, S., Dias, A., Frege, C., Hoppel, N., Troestl, J., Wagner, R., Yan, C., Amorim, A., Baltensperger, U., Curtius, J., Donahue, N. M., Gallagher, M. W., Kirkby, J., Kulmala, M., Mohler, O., Saathoff, H., Schnaiter, M., Tome, A., Virtanen, A., Worsnop, D., and Stratmann, F.: Heterogeneous ice nucleation of viscous secondary organic aerosol produced from ozonolysis of alpha-pinene, Atmospheric Chemistry and Physics, 16, 6495-6509, 10.5194/acp-16-6495-2016, 2016.

IPCC: Climate Change 2013: The Physical Science Basis. Contribution of Working Group I to the Fifth Assessment Report of the Intergovernmental Panel on Climate Change, Cambridge University Press, Cambridge, United Kingdom and New York, NY, USA, 1535 pp., 2013.

Jensen, E. J., Diskin, G., Lawson, R. P., Lance, S., Bui, T. P., Hlavka, D., McGill, M., Pfister, L., Toon, O. B., and Gao, R.: Ice nucleation and dehydration in the

Tropical Tropopause Layer, Proc Natl Acad Sci U S A, 110, 2041-2046, 10.1073/pnas.1217104110, 2013.

Joos, H., Spichtinger, P., Lohmann, U., Gayet, J. F., and Minikin, A.: Orographic cirrus in the global climate model ECHAM5. Journal of Geophysical Research: Atmospheres, 113(D18), 2008.

Kärcher, B., Hendricks, J., and Lohmann, U.: Physically based parameterization of cirrus cloud formation for use in global atmospheric models, Journal of Geophysical Research, 111, 10.1029/2005jd006219, 2006.

Kärcher, B., and Lohmann, U.: A parameterization of cirrus cloud formation: Homogeneous freezing of supercooled aerosols, Journal of Geophysical Research: Atmospheres, 107, AAC 4-1-AAC 4-10, 2002.

Knopf, D. A., Alpert, P. A., and Wang, B.: The Role of Organic Aerosol in Atmospheric Ice Nucleation: A Review, ACS Earth and Space Chemistry, 2, 168-202, 10.1021/acsearthspacechem.7b00120, 2018.

Koehler, K. A., DeMott, P. J., Kreidenweis, S. M., Popovicheva, O. B., Petters, M. D., Carrico, C. M., Kireeva, E. D., Khokhlova, T. D., and Shonija, N. K.: Cloud condensation nuclei and ice nucleation activity of hydrophobic and hydrophilic soot particles, Physical Chemistry Chemical Physics, 11, 7906-7920, 2009.

Koop, T., Luo, B. P., Tsias, A., and Peter, T.: Water activity as the determinant for homogeneous ice nucleation in aqueous solutions, Nature, 406, 611-614, 10.1038/35020537, 2000.

Koop, T., Bookhold, J., Shiraiwa, M., and Poschl, U.: Glass transition and phase state of organic compounds: dependency on molecular properties and implications for secondary organic aerosols in the atmosphere, Phys Chem Chem Phys, 13, 19238-19255, 10.1039/c1cp22617g, 2011.

Krämer, M., Schiller, C., Afchine, A., Bauer, R., Gensch, I., Mangold, A., Schlicht, S., Spelten, N., Sitnikov, N., and Borrmann, S.: Ice supersaturations and cirrus cloud crystal numbers, Atmospheric Chemistry and Physics, 9, 3505-3522, 2009.

Krämer, M., Rolf, C., Luebke, A., Afchine, A., Spelten, N., Costa, A., Meyer, J., Zoeger, M., Smith, J., and Herman, R. L.: A microphysics guide to cirrus clouds-Part 1: Cirrus types, Atmospheric Chemistry and Physics, 16, 3463-3483, 2016.

Krämer, M., C. Rolf, N. Spelten, A. Afchine, D. Fahey, E. Jensen, S. Khaykin, T. Kuhn, P. Lawson, and A. Lykov: A Microphysics Guide to Cirrus–Part II: Climatologies of Clouds and Humidity from Observations, *Atmospheric Chemistry and Physics Discussions*, doi:10.5194/acp-2020-40, 2020.

Kuebbeler, M., Lohmann, U., Hendricks, J., and Kärcher, B.: Dust ice nuclei effects on cirrus clouds, Atmos. Chem. Phys, 14, 3027-3046, 2014.

Kristjánsson, J. E., J. M. Edwards, and D. L. Mitchell: Impact of a new scheme for optical properties of ice crystals on climates of two gems. J. Geophys. Res., 105, 10 063–10 079, 2000.

Li, J. L. F., Waliser, D. E., Chen, W. T., Guan, B., Kubar, T., Stephens, G., Ma, H. Y., Deng, M., Donner, L., Seman, C., and Horowitz, L.: An observationally based evaluation of cloud ice water in CMIP3 and CMIP5 GCMs and contemporary reanalyses using contemporary satellite data, Journal of Geophysical Research-Atmospheres, 117, 10.1029/2012jd017640, 2012.

Liu, X., and Penner, J. E.: Ice nucleation parameterization for global models, Meteorologische Zeitschrift, 14, 499-514, 2005.Liu, X., Easter, R. C., Ghan, S. J., Zaveri, R., Rasch, P., Shi, X., Lamarque, J. F., Gettelman, A., Morrison, H., Vitt, F., Conley, A., Park, S., Neale, R., Hannay, C., Ekman, A. M. L., Hess, P., Mahowald, N., Collins, W., Iacono, M. J., Bretherton, C. S., Flanner, M. G., and Mitchell, D.: Toward a minimal representation of aerosols in climate models: description and evaluation in the Community Atmosphere Model CAM5, Geoscientific Model Development, 5, 709-739, 10.5194/gmd-5-709-2012, 2012.

Liu, X., Penner, J. E., and Herzog, M.: Global modeling of aerosol dynamics: Model description, evaluation, and interactions between sulfate and nonsulfate aerosols, Journal of Geophysical Research: Atmospheres, 110, 2005.Liu, X., and Shi, X.: Sensitivity of homogeneous ice nucleation to aerosol perturbations and its implications for aerosol indirect effects through cirrus clouds, Geophysical Research Letters, 45, 1684-1691, 2018.

Lohmann, U., von Salzen, K., McFarlane, N., Leighton, H. G., and Feichter, J.: Tropospheric sulfur cycle in the Canadian general circulation model, Journal of Geophysical Research: Atmospheres, 104, 26833-26858, 1999.

Lohmann, U.: Possible aerosol effects on ice clouds via contact nucleation, Journal of the atmospheric sciences, 59, 647-656, 2002.

Mahrt, F., Kilchhofer, K., Marcolli, C., Grönquist, P., David, R. O., Rösch, M., Lohmann, U., and Kanji, Z. A.: The Impact of Cloud Processing on the Ice Nucleation Abilities of Soot Particles at Cirrus Temperatures, Journal of Geophysical Research: Atmospheres, 2019.

Matus, A. V. and L'Ecuyer, T. S. : The role of cloud phase in Earth's radiation budget. Journal of Geophysical Research: Atmospheres, 122(5), 2559-2578, 2017.

Pajunoja, A., Malila, J., Hao, L. Q., Joutsensaari, J., Lehtinen, K. E. J., and Virtanen, A.: Estimating the Viscosity Range of SOA Particles Based on Their Coalescence Time, Aerosol Sci. Technol., 48, I-IV, 10.1080/02786826.2013.870325, 2014.

Penner, J. E., Chen, Y., Wang, M., and Liu, X.: Possible influence of anthropogenic aerosols on cirrus clouds and anthropogenic forcing, Atmospheric Chemistry and Physics, 9, 879-896, 2009.

Penner, J. E., Zhou, C., Garnier, A., and Mitchell, D. L.: Anthropogenic Aerosol Indirect Effects in Cirrus Clouds, Journal of Geophysical Research: Atmospheres, 123, 11,652-611,677, 10.1029/2018jd029204, 2018.

Podglajen, A., Hertzog, A., Plougonven, R., and Legras, B.: Lagrangian temperature and vertical velocity fluctuations due to gravity waves in the lower stratosphere, Geophysical Research Letters, 43, 3543-3553, 2016.

Pratt, K., Murphy, S., Subramanian, R., DeMott, P., Kok, G., Campos, T., Rogers, D., Prenni, A., Heymsfield, A., and Seinfeld, J.: Flight-based chemical characterization of biomass burning aerosols within two prescribed burn smoke plumes, Atmospheric Chemistry and Physics, 11, 12549-12565, 2011.

Prenni, A. J., DeMott, P. J., Sullivan, A. P., Sullivan, R. C., Kreidenweis, S. M., and Rogers, D. C.: Biomass burning as a potential source for atmospheric ice nuclei: Western wildfires and prescribed burns, Geophysical Research Letters, 39, 2012.

Renbaum-Wolff, L., Grayson, J. W., Bateman, A. P., Kuwata, M., Sellier, M., Murray, B. J., Shilling, J. E., Martin, S. T., and Bertram, A. K.: Viscosity of alpha-pinene secondary organic material and implications for particle growth and reactivity, Proc. Natl. Acad. Sci. U. S. A., 110, 8014-8019, 10.1073/pnas.1219548110, 2013.

Richardson, M. S., DeMott, P. J., Kreidenweis, S. M., Cziczo, D. J., Dunlea, E. J., Jimenez, J. L., Thomson, D. S., Ashbaugh, L. L., Borys, R. D., Westphal, D. L., Casuccio, G. S., and Lersch, T. L.: Measurements of heterogeneous ice nuclei in the

western United States in springtime and their relation to aerosol characteristics, Journal of Geophysical Research-Atmospheres, 112, 10.1029/2006jd007500, 2007.

Saukko, E., Lambe, A. T., Massoli, P., Koop, T., Wright, J. P., Croasdale, D. R., Pedernera, D. A., Onasch, T. B., Laaksonen, A., Davidovits, P., Worsnop, D. R., and Virtanen, A.: Humidity-dependent phase state of SOA particles from biogenic and anthropogenic precursors, Atmospheric Chemistry and Physics, 12, 7517-7529, 10.5194/acp-12-7517-2012, 2012.

Shi, X., Liu, X., and Zhang, K.: Effects of pre-existing ice crystals on cirrus clouds and comparison between different ice nucleation parameterizations with the Community Atmosphere Model (CAM5), Atmospheric Chemistry and Physics, 15, 1503-1520, 10.5194/acp-15-1503-2015, 2015.

Shi, X., and Liu, X.: Sensitivity Study of Anthropogenic Aerosol Indirect Forcing through Cirrus Clouds with CAM5 Using Three Ice Nucleation Parameterizations, Journal of Meteorological Research, 32, 693-706, 10.1007/s13351-018-8011-z, 2018.

Shiraiwa, M., Li, Y., Tsimpidi, A. P., Karydis, V. A., Berkemeier, T., Pandis, S. N., Lelieveld, J., Koop, T., and Pöschl, U.: Global distribution of particle phase state in atmospheric secondary organic aerosols, Nature Communications, 8, 15002, 10.1038/ncomms15002, 2017.

Storelvmo, T.: Aerosol Effects on Climate via Mixed-Phase and Ice Clouds, Annual Review of Earth and Planetary Sciences, 45, 199-222, 10.1146/annurev-earth-060115-012240, 2017.

Tilmes, S., Lamarque, J.-F., Emmons, L. K., Kinnison, D. E., Marsh, D., Garcia, R. R., Smith, A. K., Neely, R. R., Conley, A., Vitt, F., Val Martin, M., Tanimoto, H., Simpson, I., Blake, D. R., and Blake, N.: Representation of the Community Earth System Model (CESM1) CAM4-chem within the Chemistry-Climate Model Initiative (CCMI), Geoscientific Model Development, 9, 1853-1890, 10.5194/gmd-9-1853-2016, 2016.

van Marle, M. J. E., Kloster, S., Magi, B. I., Marlon, J. R., Daniau, A.-L., Field, R. D., Arneth, A., Forrest, M., Hantson, S., Kehrwald, N. M., Knorr, W., Lasslop, G., Li, F., Mangeon, S., Yue, C., Kaiser, J. W., and van der Werf, G. R.: Historic global biomass burning emissions for CMIP6 (BB4CMIP) based on merging satellite observations with proxies and fire models (1750–2015), Geoscientific Model Development, 10, 3329-3357, 10.5194/gmd-10-3329-2017, 2017.

Wagner, R., Höhler, K., Huang, W., Kiselev, A., Möhler, O., Mohr, C., Pajunoja, A., Saathoff, H., Schiebel, T., Shen, X., and Virtanen, A.: Heterogeneous ice nucleation of α-pinene SOA particles before and after ice cloud processing, Journal of Geophysical Research: Atmospheres, 122, 4924-4943, 10.1002/2016jd026401, 2017.

Waliser, D. E., Li, J. L. F., Woods, C. P., Austin, R. T., Bacmeister, J., Chern, J., Del Genio, A., Jiang, J. H., Kuang, Z., and Meng, H.: Cloud ice: A climate model challenge with signs and expectations of progress, Journal of Geophysical Research: Atmospheres, 114, 2009.

Wang, B., Lambe, A. T., Massoli, P., Onasch, T. B., Davidovits, P., Worsnop, D. R., and Knopf, D. A.: The deposition ice nucleation and immersion freezing potential of amorphous secondary organic aerosol: Pathways for ice and mixed-phase cloud formation, Journal of Geophysical Research: Atmospheres, 117, 2012.

Wang, M., Liu, X., Zhang, K., and Comstock, J. M.: Aerosol effects on cirrus through ice nucleation in the Community Atmosphere Model CAM5 with a statistical cirrus scheme, Journal of Advances in Modeling Earth Systems, 6, 756-776, 10.1002/2014ms000339, 2014.Wang, M., and Penner, J. E.: Aerosol indirect forcing in a global model with particle nucleation, Atmospheric Chemistry and Physics, 9, 239-260, 2009.

Wang, M., and Penner, J. E.: Cirrus clouds in a global climate model with a statistical cirrus cloud scheme, Atmospheric Chemistry and Physics, 10, 5449-5474, 10.5194/acp-10-5449-2010, 2010.

Wang, P. H., Minnis, P., McCormick, M. P., Kent, G. S., and Skeens, K. M.: A 6-year climatology of cloud occurrence frequency from Stratospheric Aerosol and Gas Experiment II observations (1985 – 1990), Journal of Geophysical Research: Atmospheres, 101, 29407-29429, 1996.

Wilson, T. W., Murray, B. J., Wagner, R., Möhler, O., Saathoff, H., Schnaiter, M., Skrotzki, J., Price, H. C., Malkin, T. L., Dobbie, S., and Al-Jumur, S. M. R. K.: Glassy aerosols with a range of compositions nucleate ice heterogeneously at cirrus temperatures, Atmospheric Chemistry and Physics, 12, 8611-8632, 10.5194/acp-12-8611-2012, 2012.

Wilkerson, J. T., Jacobson, M. Z., Malwitz, A., Balasubramanian, S., Wayson, R., Fleming, G., Naiman, A. D., and Lele, S. K.: Analysis of emission data from global

commercial aviation: 2004 and 2006, Atmos. Chem. Phys., 10, 6391–6408, https://doi.org/10.5194/acp-10-6391-2010, 2010.

Yun, Y., Penner, J. E., and Popovicheva, O.: The effects of hygroscopicity on ice nucleation of fossil fuel combustion aerosols in mixed-phase clouds, Atmospheric Chemistry and Physics, 13, 4339-4348, 10.5194/acp-13-4339-2013, 2013.

Zender, C. S., Bian, H., and Newman, D.: Mineral Dust Entrainment and Deposition (DEAD) model: Description and 1990s dust climatology, Journal of Geophysical Research: Atmospheres, 108, 2003.

Zhang, K., Wan, H., Liu, X., Ghan, S. J., Kooperman, G. J., Ma, P.-L., Rasch, P. J., Neubauer, D., and Lohmann, U.: On the use of nudging for aerosol–climate model intercomparison studies, Atmospheric Chemistry and Physics, 14, 8631-8645, 2014.

Zhou, C., and Penner, J. E.: Aircraft soot indirect effect on large-scale cirrus clouds: Is the indirect forcing by aircraft soot positive or negative?, Journal of Geophysical Research-Atmospheres, 119, 11303-11320, 10.1002/2014jd021914, 2014.

Zhou, C., Penner, J. E., Lin, G., Liu, X., and Wang, M.: What controls the low ice number concentration in the upper troposphere?, Atmospheric Chemistry and Physics, 16, 12411-12424, 10.5194/acp-16-12411-2016, 2016.

Zhu, J., and Penner, J. E.: Global Modeling of Secondary Organic Aerosol With Organic Nucleation, Journal of Geophysical Research: Atmospheres, 124, 8260-8286, 2019.

Zhu, J., and Penner, J. E.: Indirect effects of secondary organic aerosol on cirrus clouds, Journal of Geophysical Research: Atmospheres,10.1029/2019JD032233, 2020.

Zhu, J., Penner, J. E., Lin, G., Zhou, C., Xu, L., and Zhuang, B.: Mechanism of SOA formation determines magnitude of radiative effects, Proc Natl Acad Sci U S A, 114, 12685-12690, 10.1073/pnas.1712273114, 2017.

Zhu, J., Penner, J. E., Yu, F., Sillman, S., Andreae, M. O., and Coe, H.: Decrease in radiative forcing by organic aerosol nucleation, climate, and land use change, Nature Communications, 10, 423, 10.1038/s41467-019-08407-7, 2019.

Tables

Table 1. Summary of assumptions for aerosols to be effective INPs in the model

Aerosol component	Assumption to be effective INPs
Fossil/bio-fuel OM/BC	0.05% of fSootwith <1 monolayers of sulfate and 0.1% with 1-3 monolayers of sulfate when RHi reaches 120%
Biomass OM/BC	0.1% of bSoot when RHi reaches 120%
Aircraft OM/BC	Pre-activated aircraft soot within contrails with less than 3 monolayers of sulfate when RHi reaches 120%
Dust	Dust with fewer than 3 monolayers of sulfate coating when RHi reaches 120%
SOA	The newly formed SOA grow to the accumulation mode and meets the requirements of the glass transition temperature and RHi calculated using the equations in Wang et al. (2012) when RHi reaches 120%

1163

1164   Table 2. Description of cases

Case name	Description
PD_Base	Emissions for the present day (≈2000) for anthropogenic sulfur, surface and aircraft soot
PI_cSoot	As in PD_Base without INPs from pre-activated aircraft soot in contrails
PI_SO4	As in PD_Base, but with the anthropogenic sulfur emission for the preindustrial period (≈1750)
PI_ALL	As in PD_Base, but with the anthropogenic sulfur emission and surface soot emission for the pre-industrial period (≈1750) and without aircraft soot
PD_SOA	As in PD_Base, but adding INPs from newly formed SOA particles in present day
PI_SOA	As in PI_ALL, but adding INPs from newly formed SOA particles in preindustrial period

1165   Note: SOA=secondary organic aerosol; INP=ice nucleating particle.

1166

1167 Table 3. Forcing and cloud changes associated with changes in aircraft soot, sulfur
1168 and all anthropogenic aerosols.

Parameter	PD_Base-PI_cSoot	PD_Base-PI_SO4	PD_Base-PI_ALL	PD_SOA-PI_SOA
Ni (10^7 m^{-2})	-1.00±2.40	*7.26±2.88*	4.93±1.80	*11.96±2.29*
IWP (g m^{-2})	-0.13±0.06	0.07±0.06	-0.13±0.04	-0.12±0.05
LWP (g m^{-2})	-0.19±0.04	0.16±0.07	-0.05±0.08	0.03±0.06
SRF (W m^{-2})	0.35±0.13	-0.36±0.10	0.10±0.06	-0.14±0.11
LRF (W m^{-2})	*-0.49±0.09*	*0.33±0.05*	*-0.30±0.06*	0.10±0.04
NRF (W m^{-2})	-0.14±0.07	-0.02±0.06	-0.20±0.05	-0.04±0.08

1169 Note: Differences significant at the 90% level according to a Student's t test are
1170 italic.

1171

1172 **Figures**

1173

1174
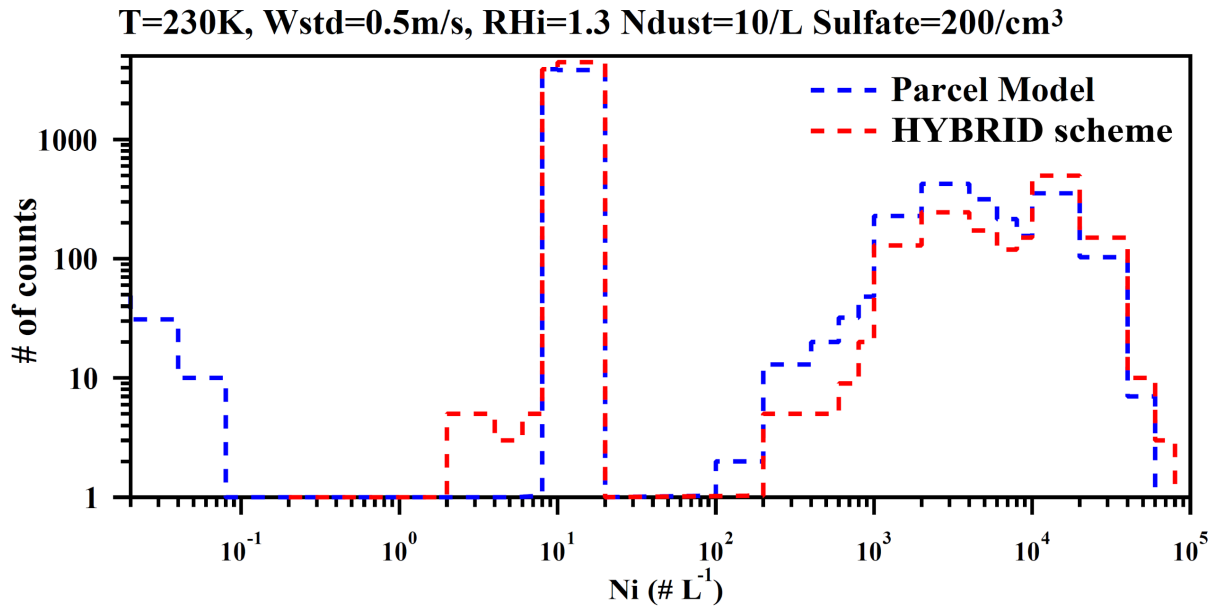
1175 Figure 1. Histogram of predicted ice number concentration for 10,000 simulations

1176 using an adiabatic parcel model (blue dashed line) and a box model using the

1177 HYBRID scheme (red dashed line). Wstd is the standard deviation of the assumed

1178 pdf of updraft velocities, while Ndust and Sulfate are the assumed dust and sulfate

1179 number concentrations.

1180

1181

1182
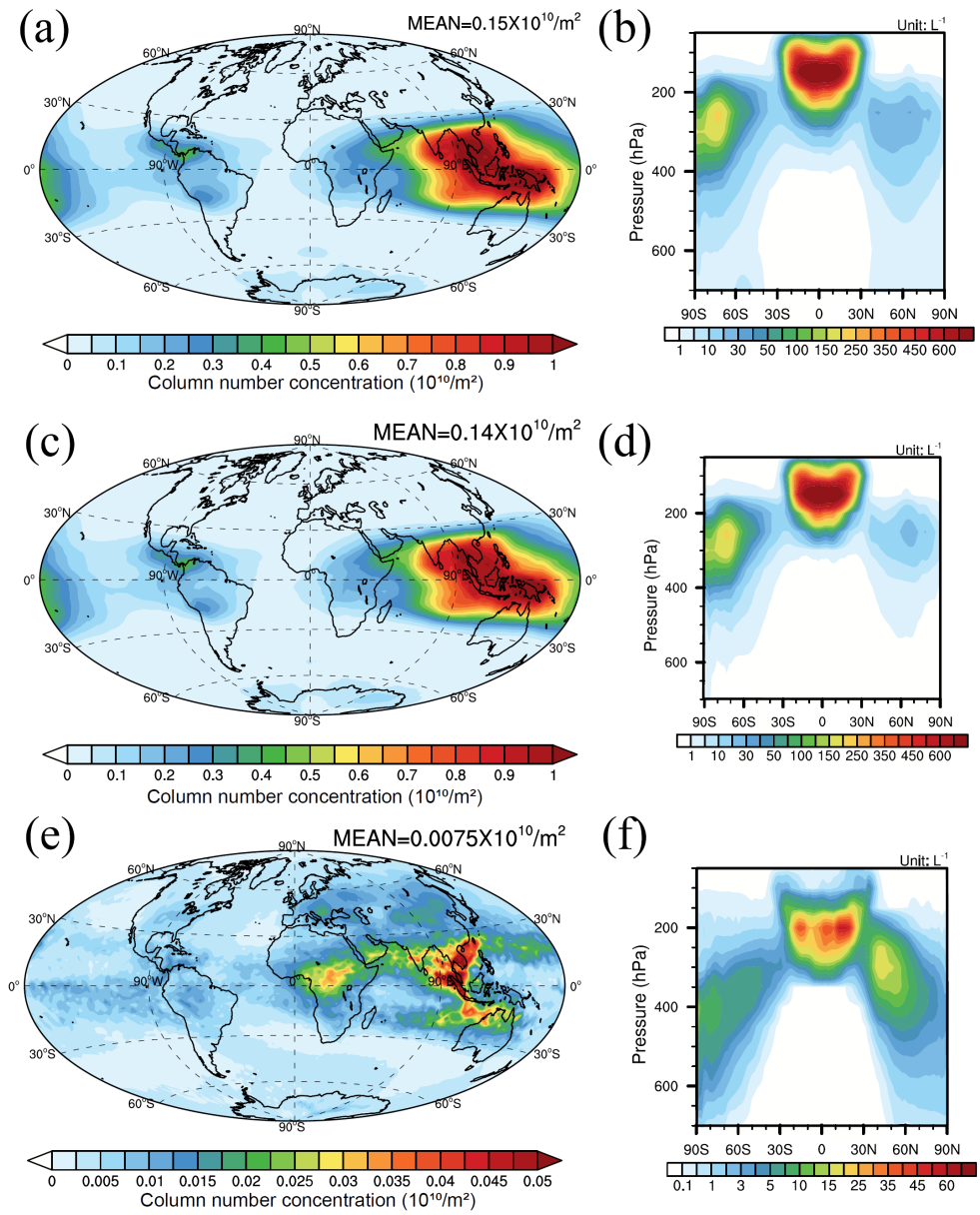
Figure 2. The vertically integrated total Ni in PD_Base case (a), Ni from

homogeneous nucleation (c) and Ni from heterogeneous nucleation (e). The zonal

average plots of Ni in PD_Base case (b), Ni from homogeneous nucleation (d) and

Ni from heterogeneous nucleation (f). Note: the vertical axis in (b), (d) and (f) are

in hybrid pressure levels
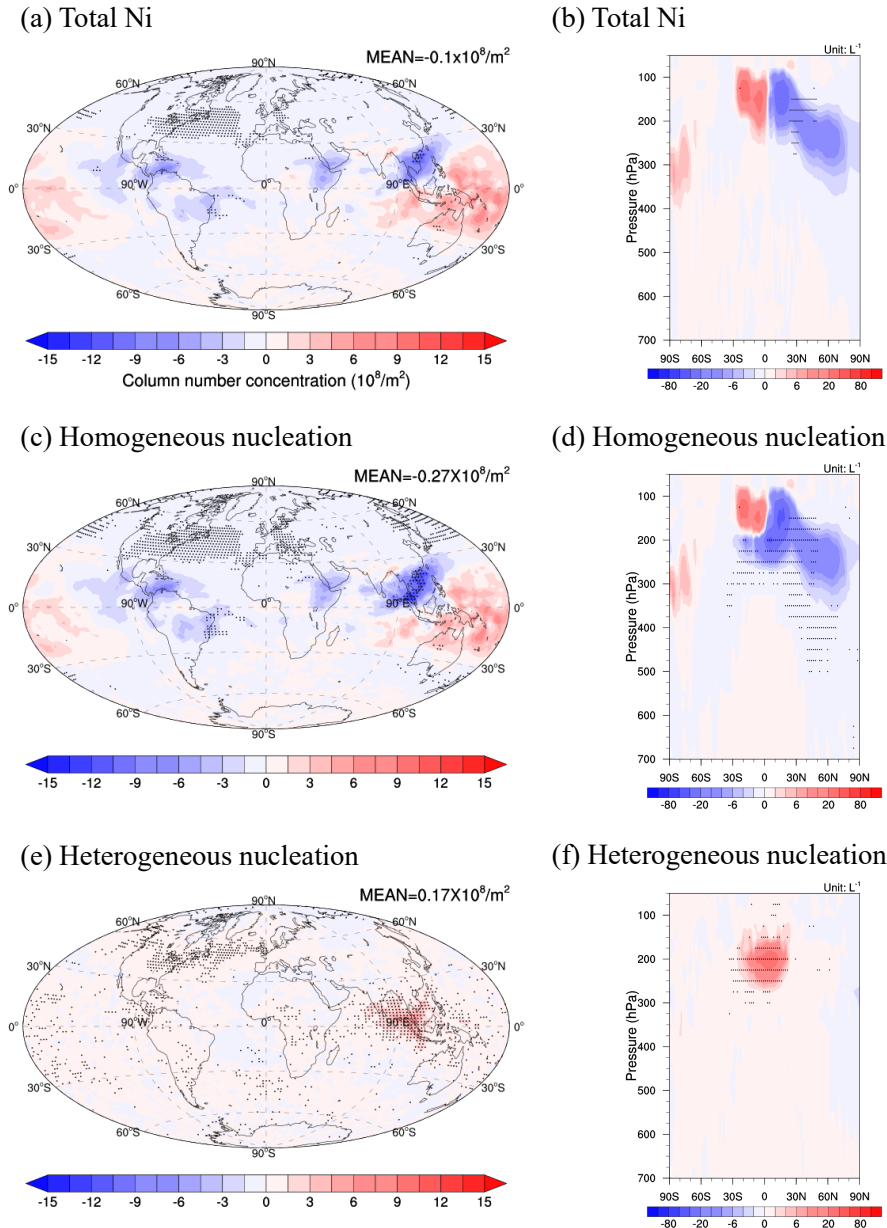
Figure 3. The annual average change in column number concentration (a, c, e) and zonal average number concentration (b, d, f) of total ice (a, b), ice from homogeneous nucleation (c, d) and ice from heterogeneous nucleation (e, f) for the difference between the PD_Base and PI_cSoot cases. Differences significant at the 90% level according to a Student's t test are depicted by points.
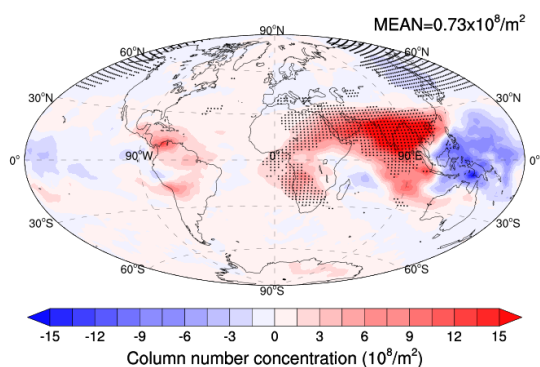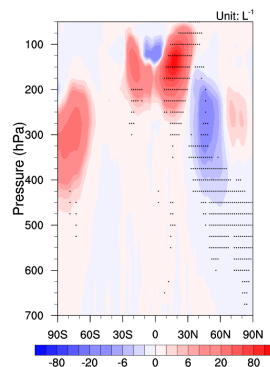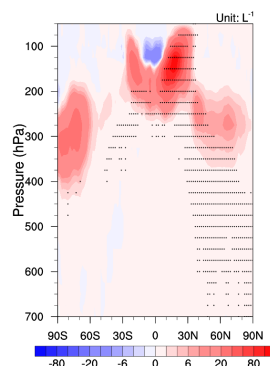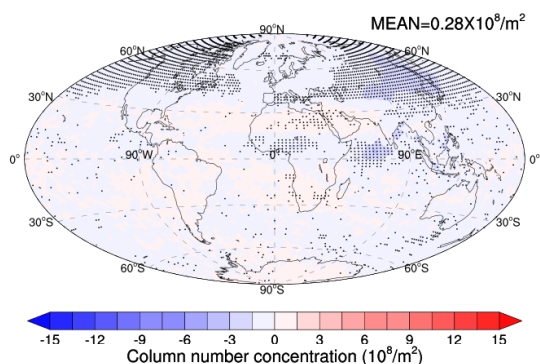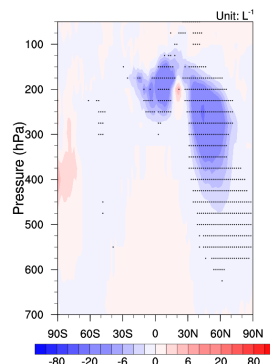
Figure 4. As in Figure 3 but for the difference between the PD_Base and PI_SO4 cases. Differences significant at the 90% level according to a Student's t test are depicted by points.
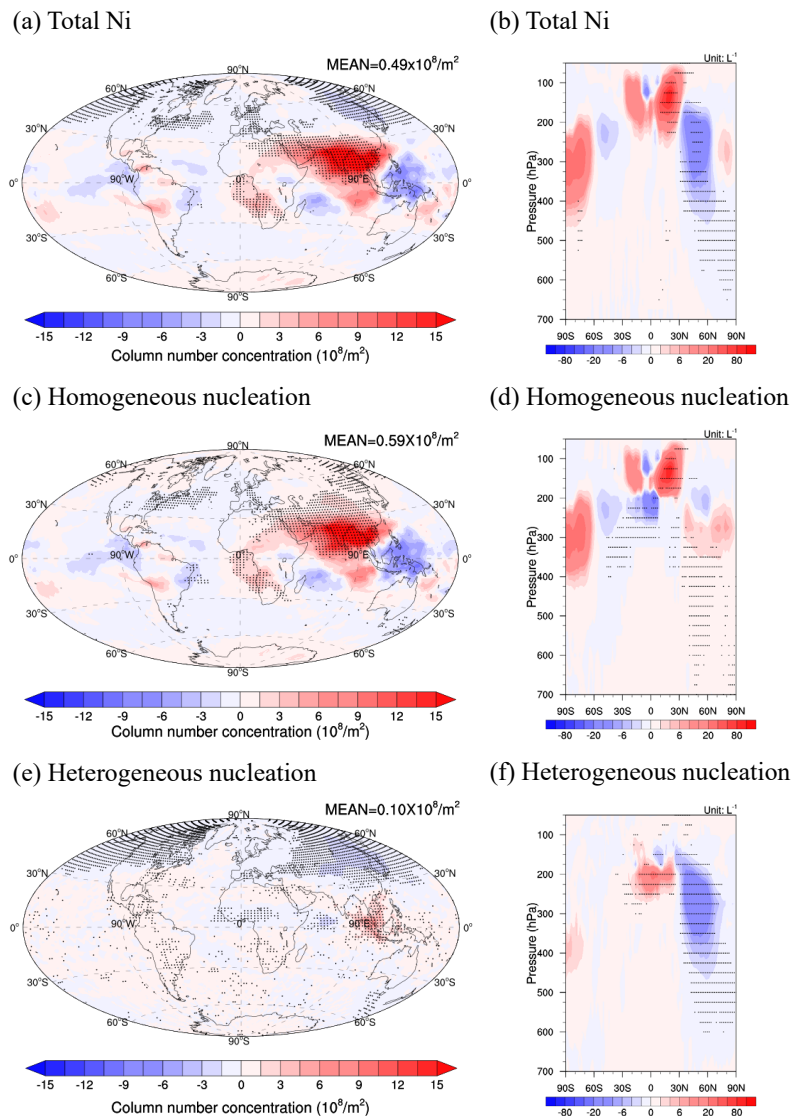
Figure 5. As in Figure 3 but for the difference between the PD_Base and PI_ALL cases. Differences significant at the 90% level according to a Student's t test are depicted by points.
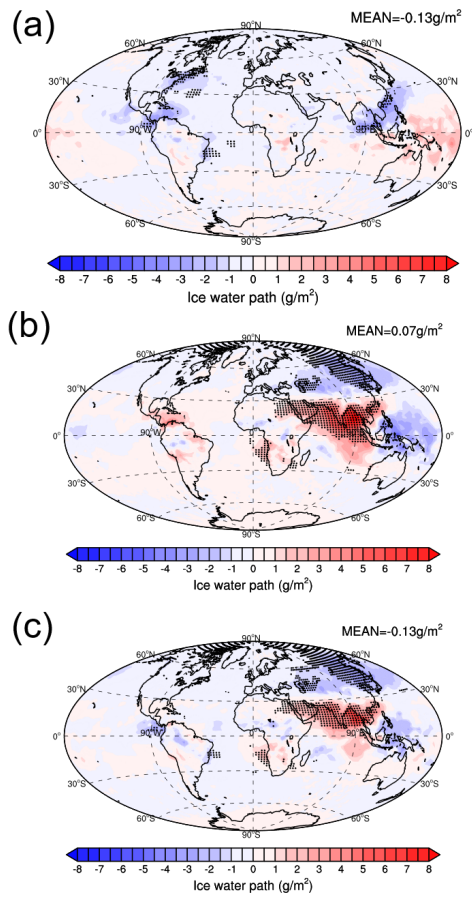
1206

1207   Figure 6. Annual mean plots of the change in vertically integrated averaged ice

1208   water path for the difference between the PD_Base and PI_cSoot cases (a),

1209   PD_Base and PI_SO4 cases (b) as well as the PD_Base and PI_ALL cases (c).

1210   Differences significant at the 90% level according to a Student's t test are depicted

1211   by points.

1212
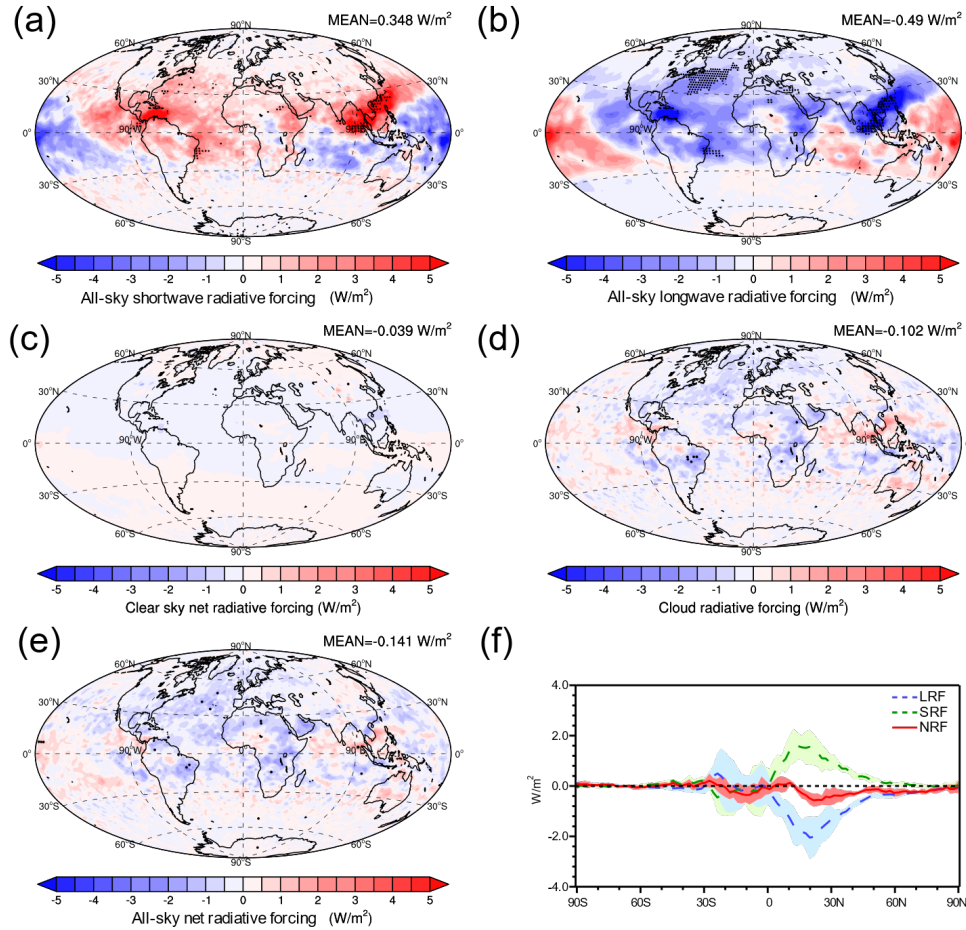
1213

Figure 7. Annual mean plots of all-sky shortwave radiative forcing (a), all-sky

longwave radiative forcing (b), clear sky net radiative forcing (c), cloud radiative

forcing (d) and all-sky net radiative forcing (e) as well as all-sky longwave

radiative forcing (f, LRF, blue dashed line), all-sky shortwave radiative forcing (f,

SRF, green dashed line) and all-sky net radiative forcing (f, NRF, red solid line)

versus latitude for the difference between the PD_Base and PI_cSoot cases.

Differences significant at the 90% level according to a Student's t test are depicted

by points. The shading in (f) represents one standard deviation of the interannual

variation over six years.

1223

1224
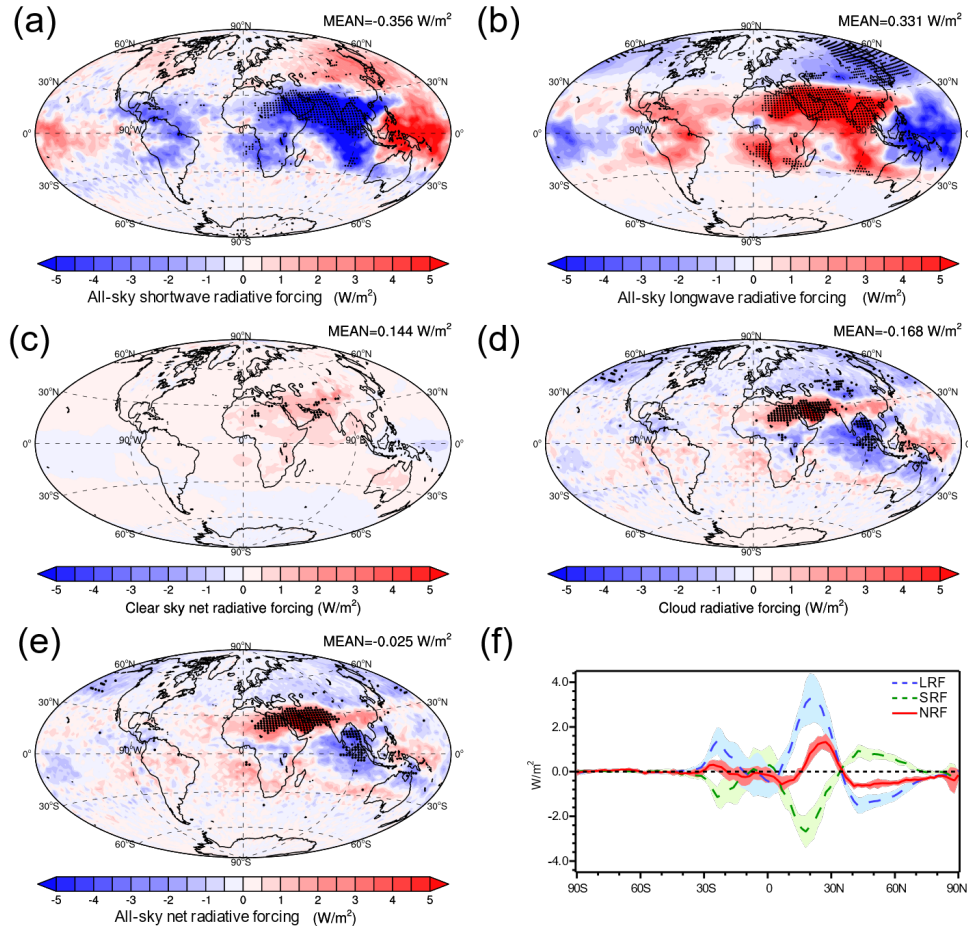
Figure 8. As in Figure 7 but for the difference between the PD_Base and PI_SO4

cases. Differences significant at the 90% level according to a Student's t test are

depicted by points. The shading in (f) represents one standard deviation of the

interannual variation over six years.

1229

1230

1231
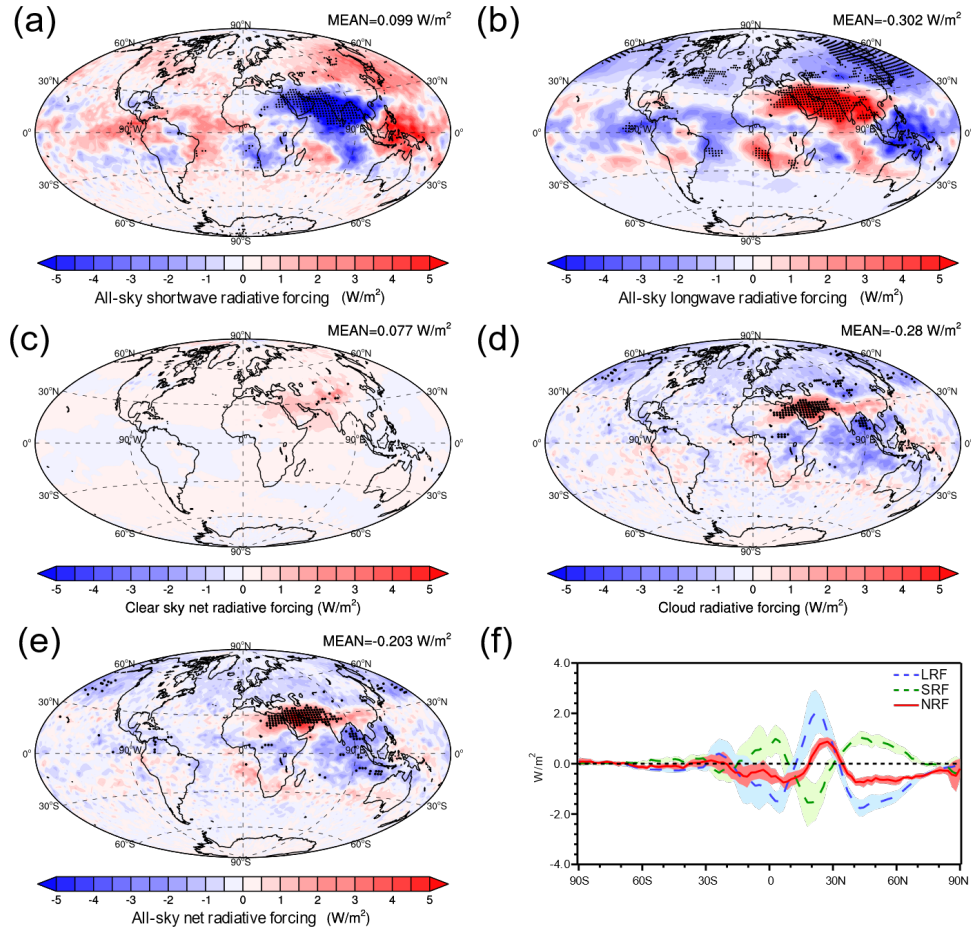
Figure 9. As in Figure 7 but for the difference between the PD_Base and PI_ALL

cases. Differences significant at the 90% level according to a Student's t test are

depicted by points. The shading in (f) represents one standard deviation of the

interannual variation over six years.

1236

1237

1238

1239
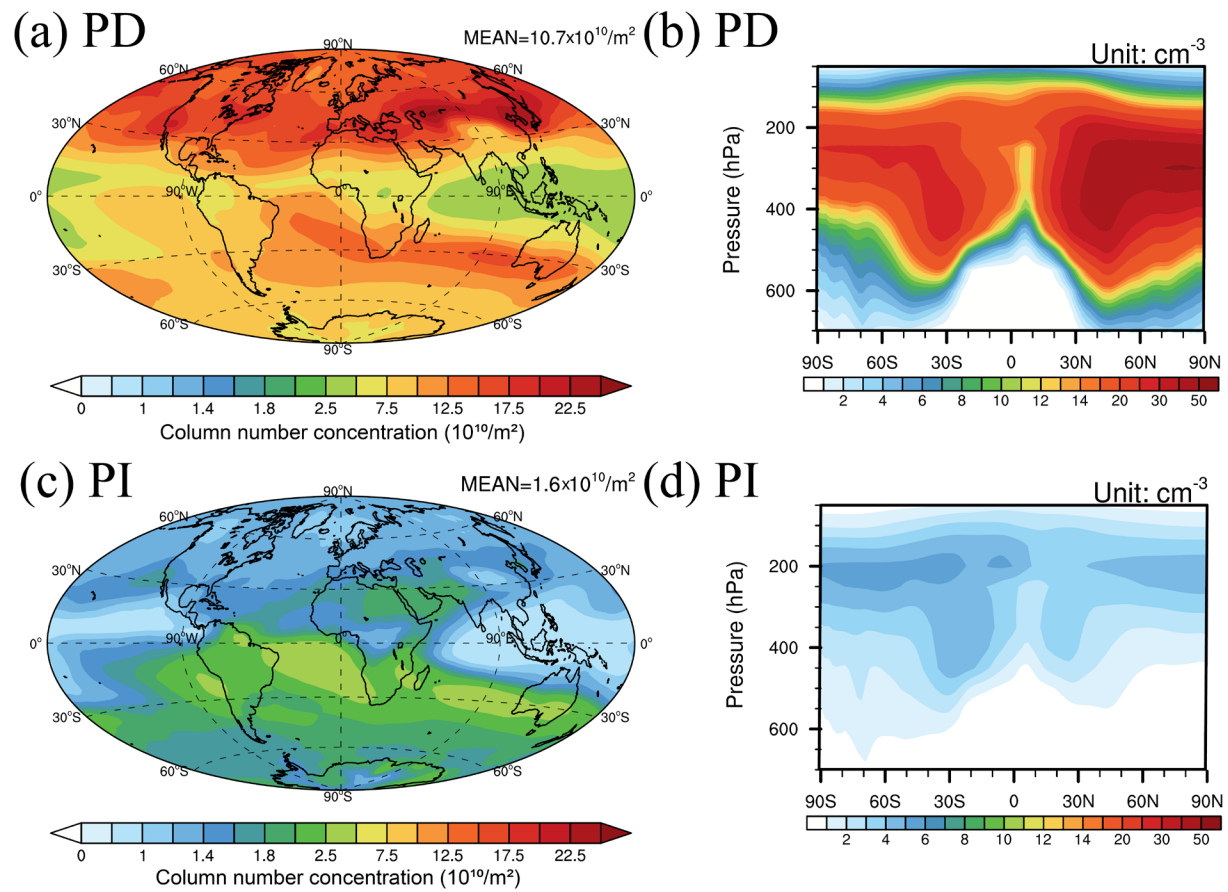
1240   Figure 10. The vertically integrated number of INP (a, c) and zonal average plots

1241   of INP (b, d) from SOA in the PD_SOA (a, b) and PI_SOA (c, d) cases.
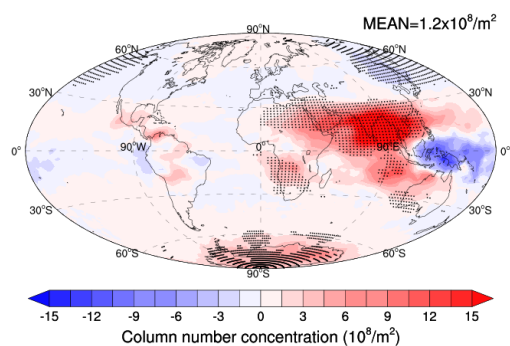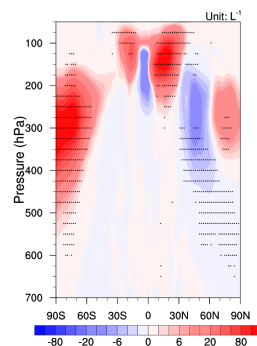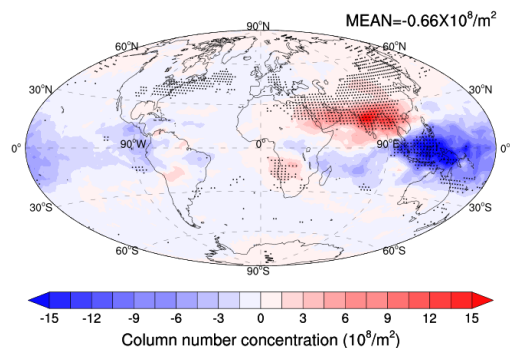
1242

1243
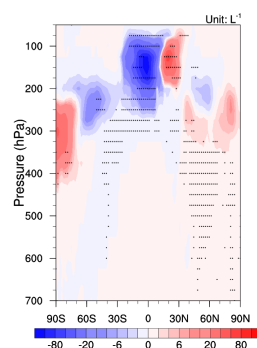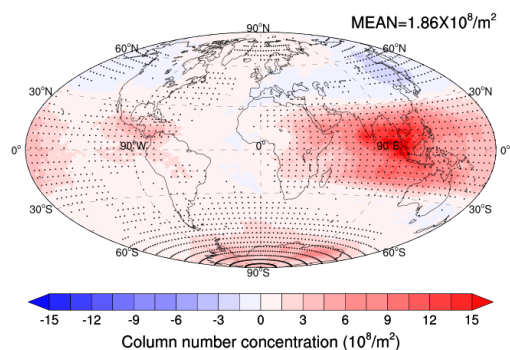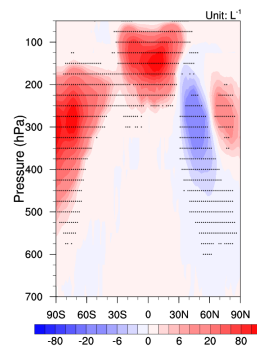
1244

Figure 11. The annual average change in column number concentration (a, c, e) and zonal average number concentration (b, d, f) of total ice (a, b), ice from homogeneous nucleation (c, d) and ice from heterogeneous nucleation (e, f) for the difference between the PD_SOA and PI_SOA cases. Differences significant at the 90% level according to a Student's t test are depicted by points.

1245

1246

1247

1248

1249

1250

1251
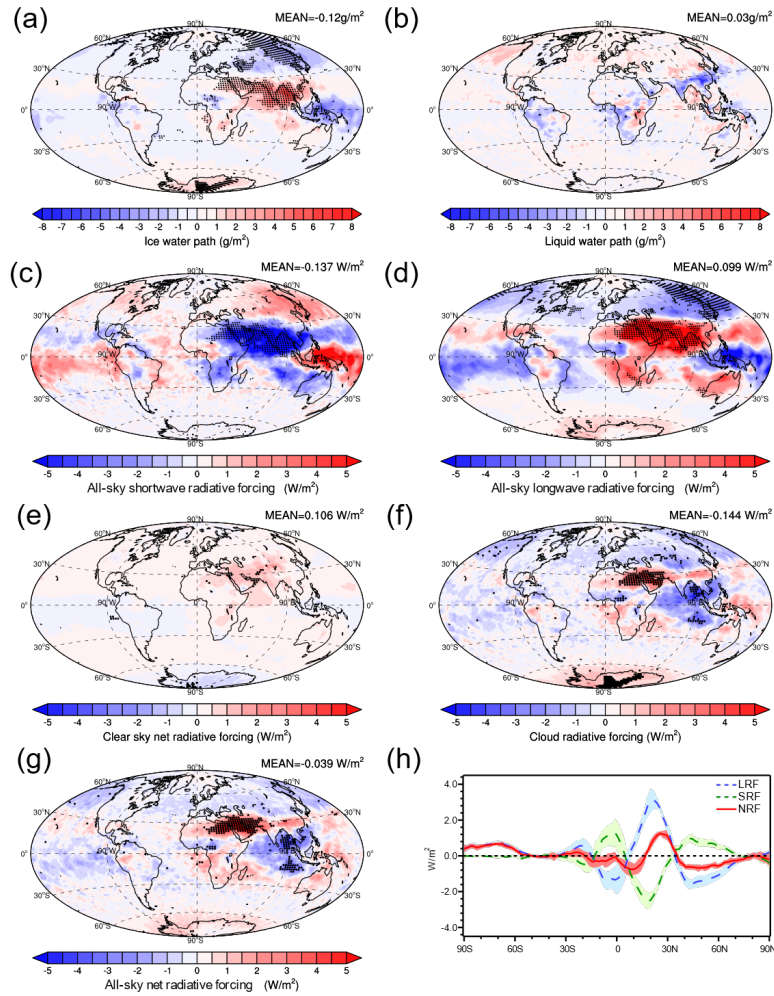
Figure 12. Annual mean plots of the changes in ice water path (a), liquid water
path (b), all-sky shortwave radiative forcing (c), all-sky longwave radiative forcing
(d), clear sky net radiative forcing (e), cloud radiative forcing (f) and all-sky net
radiative forcing (g) as well as longwave radiative forcing (h, LRF, blue dashed
line), shortwave radiative forcing (h, SRF, green dashed line) and all-sky net
radiative forcing (h, NRF, red solid line) versus latitude for the difference between
the PD_SOA and PI_SOA cases. Differences significant at the 90% level
according to a Student's t test are depicted by points. The shading in (h) represents
one standard deviation of the interannual variation over six years.

1261
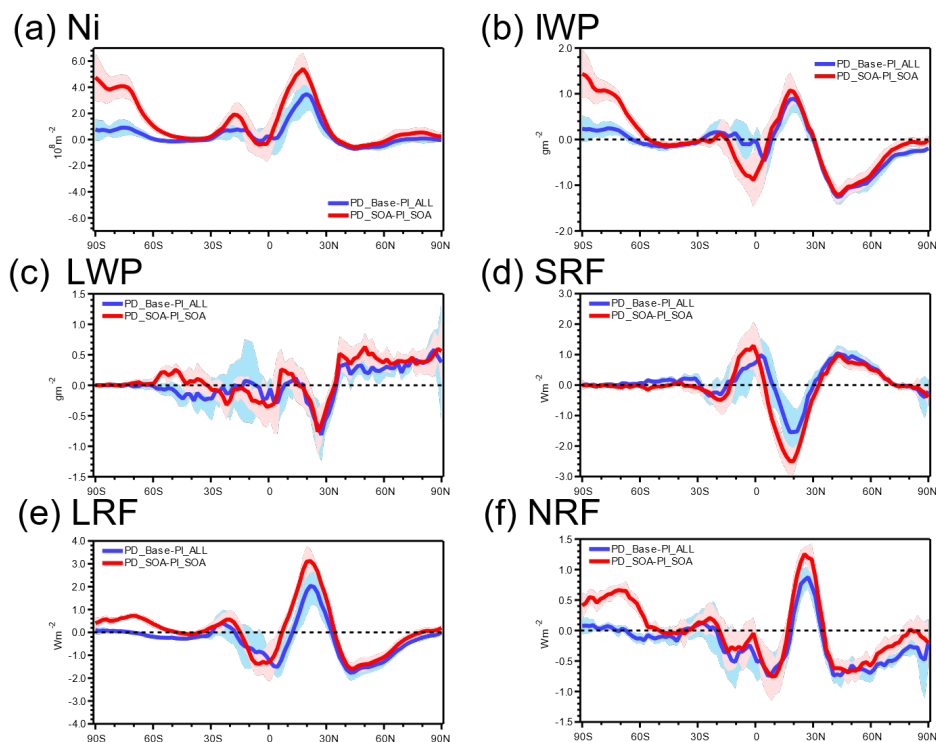
1262 Figure 13. Change in vertically integrated ice number concentration (a), ice water

1263 path (b), liquid water path (c) as well as shortwave radiative forcing (d), longwave

1264 radiative foricng (e) and all-sky net radiative forcing (f) for the difference between

1265 the PD_SOA and PI_SOA cases (red line) as well as PD_Base and PI_ALL cases

1266 (blue line). The shading represents one standard deviation of the interannual

1267 variation over six years.

1268

1269

1270

1271

1272